Search for additional heavy neutral Higgs and gauge bosons in the ditau final state produced in $36.1\,\text{fb}^{-1}$ of pp collisions at $\sqrt{s} = 13\,\text{TeV}$ with the ATLAS detector

The ATLAS Collaboration

A search for neutral Higgs bosons of the Minimal Supersymmetric Standard Model (MSSM) and for heavy neutral Z' bosons is performed using a data sample corresponding to an integrated luminosity of $36.1\,\text{fb}^{-1}$ from proton-proton collisions at $\sqrt{s} = 13\,\text{TeV}$ recorded by the ATLAS detector at the LHC during 2015 and 2016. The heavy resonance is assumed to decay to $\tau^+\tau^-$ with at least one tau lepton decaying to final states with hadrons and a neutrino. The search is performed in the mass range of 0.2–2.25 TeV for the MSSM neutral Higgs bosons and 0.2–4.0 TeV for the heavy neutral Z' boson. The data are in good agreement with the background predicted by the Standard Model. The results are interpreted in MSSM and Z' benchmark scenarios. In the context of the hMSSM scenario, the most stringent limits for the combined search exclude $\tan\beta > 1.0$ for $m_A = 0.25\,\text{TeV}$ and $\tan\beta > 45$ for $m_A = 1.5\,\text{TeV}$ at the 95% confidence level (CL). For the Sequential Standard Model, a Z'_{SSM} mass up to 2.42 TeV is excluded at 95% CL and masses up to 2.25–2.60 TeV are excluded for a Z'_{SFM} of the Strong Flavour Model.

1 Introduction

The discovery of a scalar particle [1, 2] at the Large Hadron Collider (LHC) [3] has provided important insight into the mechanism of electroweak symmetry breaking. Experimental studies of the new particle [4–8] demonstrate consistency with the Standard Model (SM) Higgs boson [9–14]. However, it remains possible that the discovered particle is part of an extended scalar sector, a scenario that is favoured by a number of theoretical arguments [15, 16].

The Minimal Supersymmetric Standard Model (MSSM) [15, 17, 18] is the simplest extension of the SM that includes Supersymmetry. The MSSM requires two Higgs doublets of opposite hypercharge. Assuming that CP symmetry is conserved, this results in one CP-odd (A) and two CP-even (h, H) neutral Higgs bosons and two charged Higgs bosons ($H^{\pm}$). At tree level, the properties of the Higgs sector in the MSSM depend on only two non-SM parameters, which can be chosen to be the mass of the CP-odd Higgs boson, m_A, and the ratio of the vacuum expectation values of the two Higgs doublets, $\tan\beta$. Beyond tree level, a number of additional parameters affect the Higgs sector, the choice of which defines various MSSM benchmark scenarios. In some scenarios, such as $m_h^{\mathrm{mod+}}$ [19], the top-squark mixing parameter is chosen such that the mass of the lightest CP-even Higgs boson, m_h, is close to the measured mass of the Higgs boson that was discovered at the LHC. A different approach is employed in the hMSSM scenario [20, 21] in which the measured value of m_h can be used, with certain assumptions, to predict the remaining masses and couplings of the MSSM Higgs bosons without explicit reference to the soft supersymmetry-breaking parameters. The couplings of the MSSM heavy Higgs bosons to down-type fermions are enhanced with respect to the SM Higgs boson for large $\tan\beta$ values, resulting in increased branching fractions to τ-leptons and b-quarks, as well as a higher cross section for Higgs boson production in association with b-quarks. This has motivated a variety of searches for a scalar boson (generically called ϕ) in $\tau\tau$ and bb final states[1] at LEP [22], the Tevatron [23–25] and the LHC [26–32].

Heavy Z' gauge bosons appear in several BSM models [33–36] and are a common extension of the SM [37]. Such Z' bosons are predicted in theories extending the electroweak gauge group, where lepton universality is typically conserved. A frequently used benchmark is the Sequential Standard Model (SSM) [38], which contains a single additional Z' boson with the same couplings as the SM Z boson. Furthermore, some models offering an explanation for the high mass of the top quark predict that such bosons couple preferentially to third-generation fermions [39–42]. A model predicting additional weak gauge bosons Z' and W' coupling preferentially to third-generation fermions is the Strong Flavour Model (SFM) [40, 42]. Indirect limits on Z' bosons with non-universal flavour couplings have been set based on measurements from LEP [43]. Direct searches for high-mass resonances decaying to ditau final states have been performed by the ATLAS [44] and CMS [45] collaborations using $5\,\mathrm{fb}^{-1}$ of integrated luminosity at $\sqrt{s} = 7\,\mathrm{TeV}$. ATLAS extended the reach of the search with $20\,\mathrm{fb}^{-1}$ of integrated luminosity at $\sqrt{s} = 8\,\mathrm{TeV}$ [46].

This paper presents the results of a search for neutral MSSM Higgs bosons as well as high-mass Z' resonances in the ditau decay mode using $36.1\,\mathrm{fb}^{-1}$ of proton–proton collision data at a centre-of-mass energy of $13\,\mathrm{TeV}$ collected with the ATLAS detector [47] in 2015 and 2016. The search is performed in the $\tau_{\mathrm{lep}}\tau_{\mathrm{had}}$ and $\tau_{\mathrm{had}}\tau_{\mathrm{had}}$ decay modes, where τ_{lep} represents the decay of a τ-lepton to an electron or a muon and neutrinos, whereas τ_{had} represents the decay to one or more hadrons and a neutrino. The search considers narrow resonances[2] in the mass range of 0.2–2.25 TeV and $\tan\beta$ range of 1–58 for the MSSM

---

[1] Throughout this paper the inclusion of charge-conjugate decay modes is implied.
[2] A resonance is considered "narrow" if the lineshape has no impact on experimental observables.
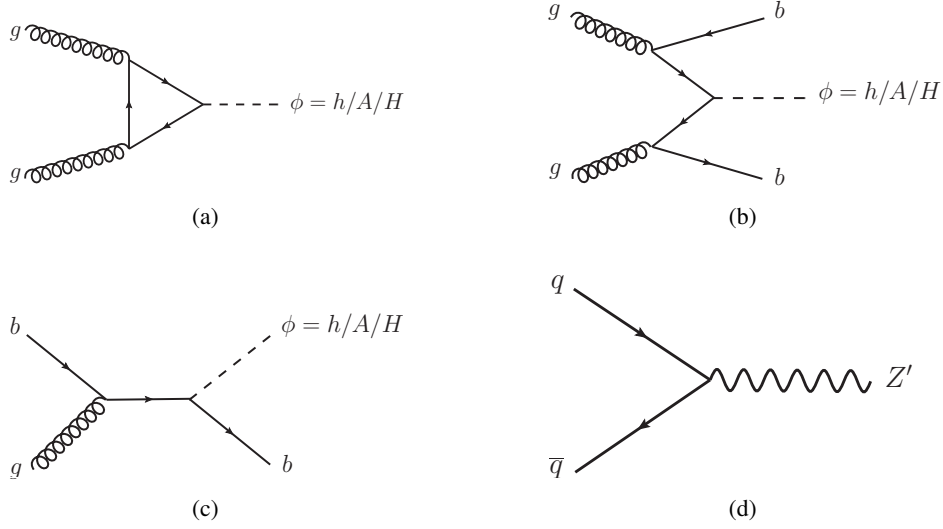
Figure 1: Lowest-order Feynman diagrams for gluon fusion (a) and b-associated production of a neutral MSSM Higgs boson in the four-flavour (b) and five-flavour (c) schemes; Feynman diagram for Drell–Yan production of a Z' boson at lowest order (d).

Higgs bosons. For the Z' boson search, a mass range of 0.2–4 TeV is considered. Higgs boson production through gluon fusion and in association with b-quarks is considered (Figures 1(a)–1(c)), with the latter mode dominating for high $\tan\beta$ values. Hence both the $\tau_{\text{lep}}\tau_{\text{had}}$ and $\tau_{\text{had}}\tau_{\text{had}}$ channels are split into b-tag and b-veto categories, based on the presence or absence of jets originating from b-quarks in the final state. Since a Z' boson is expected to be predominantly produced via a Drell–Yan process (Figure 1(d)), there is little gain in splitting the data into b-tag and b-veto categories. Hence, the Z' analysis uses an inclusive selection instead.

2 ATLAS detector

The ATLAS detector [47] at the LHC covers nearly the entire solid angle around the collision point. It consists of an inner tracking detector surrounded by a thin superconducting solenoid, electromagnetic and hadronic calorimeters, and a muon spectrometer incorporating three large superconducting toroid magnets. The inner-detector system is immersed in a 2 T axial magnetic field and provides charged particle tracking in the range $|\eta| < 2.5$.[3]

The high-granularity silicon pixel detector covers the vertex region and typically provides four measurements per track. The innermost layer, known as the Insertable B-Layer [48, 49], was added in 2014 and provides high-resolution hits at small radius to improve the tracking performance. The pixel detector is surrounded by the silicon microstrip tracker, which provides four three-dimensional measurement points

---

[3] ATLAS uses a right-handed coordinate system with its origin at the nominal interaction point in the centre of the detector and the z-axis along the beam pipe. The x-axis points from the interaction point to the centre of the LHC ring, and the y-axis points upwards. Cylindrical coordinates (r, ϕ) are used in the transverse plane, ϕ being the azimuthal angle around the z-axis. The pseudorapidity is defined in terms of the polar angle θ as $\eta = -\ln\tan(\theta/2)$. Angular distance is measured in units of $\Delta R \equiv \sqrt{(\Delta\eta)^2 + (\Delta\phi)^2}$.

per track. These silicon detectors are complemented by the transition radiation tracker, which enables radially extended track reconstruction up to $|\eta| = 2.0$. The transition radiation tracker also provides electron identification information based on the fraction of hits (typically 30 in total) above a higher energy deposit threshold corresponding to transition radiation.

The calorimeter system covers the pseudorapidity range $|\eta| < 4.9$. Within the region $|\eta| < 3.2$, electromagnetic calorimetry is provided by barrel and endcap high-granularity lead/liquid-argon (LAr) electromagnetic calorimeters, with an additional thin LAr presampler covering $|\eta| < 1.8$, to correct for energy loss in material upstream of the calorimeters. Hadronic calorimetry is provided by the steel/scintillating-tile calorimeter, segmented into three barrel structures within $|\eta| < 1.7$, and two copper/LAr hadronic endcap calorimeters that cover $1.5 < |\eta| < 3.2$. The solid angle coverage is completed with forward copper/LAr and tungsten/LAr calorimeter modules, optimised for electromagnetic and hadronic measurements respectively, in the region $3.1 < |\eta| < 4.9$.

The muon spectrometer comprises separate trigger and high-precision tracking chambers measuring the deflection of muons in a magnetic field generated by superconducting air-core toroids. The precision chamber system covers the region $|\eta| < 2.7$ with three layers of monitored drift tubes, complemented by cathode strip chambers in the forward region, where the background is highest. The muon trigger system covers the range $|\eta| < 2.4$ with resistive plate chambers in the barrel, and thin gap chambers in the endcap regions.

A two-level trigger system is used to select interesting events [50, 51]. The Level-1 trigger is implemented in hardware and uses a subset of detector information to reduce the event rate to a design value of at most 100 kHz. This is followed by the software-based high-level trigger, which reduces the event rate to 1 kHz.

3 Data samples

The results in this paper use proton-proton collision data at a centre-of-mass energy of $\sqrt{s} = 13$ TeV collected by the ATLAS detector at the LHC during 2015 and 2016. The data correspond to a total integrated luminosity of $36.1\,\mathrm{fb}^{-1}$ after requiring that all relevant components of the ATLAS detector are in good working condition. Selected events must pass criteria designed to reduce backgrounds from cosmic rays, beam-induced events and calorimeter noise [52]. They must also contain at least one primary vertex with at least two associated tracks. The primary vertex is chosen as the proton-proton vertex candidate with the highest sum of the squared transverse momenta of all associated tracks.

Simulated events are used to estimate signal efficiencies and some background contributions. The simulated samples are normalised to the expected number of events in the collected dataset via their theoretical cross sections. Simulated events with a heavy neutral MSSM Higgs boson produced via gluon fusion and in association with b-quarks are generated at NLO with POWHEG-BOX v2 [53–55] and MG5_aMC@NLO [56, 57], respectively. The CT10 [58] set of parton distribution functions (PDFs) is used in the generation of gluon fusion events while CT10nlo_nf4 [59] is used to produce the b-associated signal samples. PYTHIA 8.210 [60] with the AZNLO [61] (A14 [62]) set of tuned parameters is used together with the CTEQ6L1 [63] (NNPDF2.3LO [64]) PDF set for the parton shower calculation at LO, underlying event and hadronisation in the gluon fusion (b-associated) production. The production cross sections and branching fractions for the various MSSM scenarios are taken from Ref. [65]. The cross sections are calculated using SUSHI [66] for gluon fusion production [67–71] and b-associated production

in the five-flavour scheme [72]; b-associated production in the four-flavour scheme (where b-quarks are not considered as partons) is calculated according to Refs. [73, 74]. The final b-associated production cross section is obtained by using the method in Ref. [75] to match the four-flavour and five-flavour scheme cross sections. The masses and the couplings of the Higgs bosons are computed with FEYNHIGGS [76–79], whereas the branching fraction calculation follows the procedure described in Ref. [80]. In the case of the hMSSM scenario, the procedure described in Ref. [21] is followed for the production cross sections and HDECAY [81] is used for the branching fraction calculation.

The Z' signal events are simulated by reweighting a leading-order (LO) Z/γ^* sample using the TAUSPINNER algorithm [82–84] to account for spin effects in the τ-lepton decays. The Z/γ^* sample, enriched with high invariant mass events, is generated with PYTHIA 8.165 [85, 86] using the NNPDF2.3LO PDF set and the A14 tune for the shower and underlying event parameters. Interference between the Z' and the SM Z/γ^* production is not included, as it is highly model dependent. Higher-order Quantum Chromodynamics (QCD) corrections are applied to the simulated samples. These corrections to the event yields are done using a mass-dependent rescaling to next-to-next-to-leading order (NNLO) in the QCD coupling constant, as calculated with VRAP 0.9 [87] and the CT14NNLO PDF set [59]. Electroweak (EW) corrections are not applied to the Z' signal samples due to the large model dependence.

The simulated backgrounds consist of Z/γ^*+jets, W+jets, $t\bar{t}$, single top-quark and diboson (WW, WZ and ZZ) production. These are modelled with several event generators as described below. The multijet background in both channels is estimated using data, while non-multijet backgrounds in which a quark- or gluon-initiated jet is misidentified as a hadronic tau decay (predominantly W+jets and $t\bar{t}$) are modelled using data in the $\tau_{lep}\tau_{had}$ channel and simulation with data-driven corrections in the $\tau_{had}\tau_{had}$ channel, as described in Section 6.

Events containing Z/γ^*+jets are simulated using POWHEG-BOX v2 [88] interfaced to the PYTHIA 8.186 parton shower model. The CT10 PDF set is used in the matrix element. The AZNLO tune is used, with PDF set CTEQ6L1, for the modelling of non-perturbative effects. The EVTGEN v1.2.0 program [89] is used for properties of the bottom and charm hadron decays. PHOTOS++ 3.52 [90] is used for QED emissions from electroweak vertices and charged leptons. The same setup is used to simulate W+jets events that are used for background subtraction in control regions of the $\tau_{lep}\tau_{had}$ channel. The Z/γ^*+jets samples are simulated in slices with different masses of the off-shell boson mass. Event yields are corrected with a mass-dependent rescaling at NNLO in the QCD coupling constant, computed with VRAP 0.9 and the CT14NNLO PDF set. Mass-dependent EW corrections are computed at NLO with MCSANC 1.20 [91], and these include photon-induced contributions ($\gamma\gamma \to \ell\ell$ via t- and u-channel processes) computed with the MRST2004QED PDF set [92].

The modelling of the W+jets process in the case of the $\tau_{had}\tau_{had}$ channel is done with the SHERPA 2.2.0 [93] generator. Matrix elements are calculated for up to 2 partons at NLO and 4 partons at LO using the COMIX [94] and OPENLOOPS [95] matrix element generators and merged with the Sherpa parton shower [96] using the ME+PS@NLO prescription [97]. The CT10nlo PDF set is used in conjunction with dedicated parton shower tuning developed by the Sherpa authors. The W+jets production is normalised to the NNLO cross sections using FEWZ [98–100].

For the generation of $t\bar{t}$ and single top-quark in the Wt and s-channel the POWHEG-BOX v2 generator with the CT10 PDF sets in the matrix element calculations is used. Electroweak t-channel single top-quark events are generated using the POWHEG-BOX v1 generator. This generator uses the 4-flavour scheme for the NLO matrix elements calculations together with the fixed four-flavour PDF set CT10f4 [58]. For all top processes, top-quark spin correlations are preserved (for t-channel, top quarks are decayed

using MADSPIN [101]). The parton shower, fragmentation, and the underlying event are simulated using PYTHIA 6.428 with the CTEQ6L1 PDF sets and the corresponding Perugia 2012 tune [102]. The top mass is set to 172.5 GeV. The $t\bar{t}$ production sample is normalised to the predicted production cross section as calculated with the TOP++2.0 program to NNLO in perturbative QCD, including soft-gluon resummation to next-to-next-to-leading-log order (Ref. [103] and references therein). The normalisation of the single top-quark event samples use an approximate calculation at NLO in QCD for the s and t channels [104, 105] while NLO+NNLL predictions are used for the Wt-channel [106]. The EVTGEN v1.2.0 program is used for properties of the bottom and charm hadron decays.

Diboson processes are modelled using the SHERPA 2.1.1 generator and they are calculated for up to 1 (ZZ) or 0 (WW, WZ) additional partons at NLO and up to 3 additional partons at LO using the COMIX and OPENLOOPS matrix element generators and merged with the Sherpa parton shower using the ME+PS@NLO prescription. The CT10 PDF set is used in conjunction with dedicated parton shower tuning developed by the Sherpa authors. The generator cross sections are used in this case (already at NLO). In addition, the Sherpa diboson sample cross section has been scaled down to account for its use of $\alpha_{\mathrm{QED}} = 1/129$ rather than 1/132 corresponding to the use of current PDG parameters as input to the G_μ scheme.

Simulated minimum-bias events are overlaid on all simulated samples to include the effect of multiple proton-proton interactions in the same and neighbouring bunch crossings ("pile-up"). These minimum-bias events are generated with PYTHIA 8.186, using the A2 tune [107] and the MSTW2008LO PDF [108].

Each sample is simulated using the full GEANT 4 [109, 110] simulation of the ATLAS detector, with the exception of the b-associated MSSM Higgs boson signal, for which the ATLFASTII [110, 111] fast simulation framework is used. Finally, the simulated events are processed through the same reconstruction software as the data.

4 Event reconstruction

Electron candidates are reconstructed from energy deposits in the electromagnetic calorimeter associated with a charged-particle track measured in the inner detector [112, 113]. The electron candidates are required to pass a "loose" likelihood-based identification selection [114], to have a transverse momentum $p_{\mathrm{T}} > 15$ GeV and to be in the fiducial volume of the inner detector, $|\eta| < 2.47$. The transition region between the barrel and end-cap calorimeters ($1.37 < |\eta| < 1.52$) is excluded.

Muon candidates are reconstructed from track segments in the muon spectrometer matched with tracks found in the inner detector within $|\eta| < 2.5$ [115]. The tracks of the muon candidates are refitted using the complete track information from both detector systems. They are required to have a transverse momentum $p_{\mathrm{T}} > 7$ GeV and to pass a "loose" muon identification requirement.

The selected lepton (electron or muon) in the $\tau_{\mathrm{lep}}\tau_{\mathrm{had}}$ channel must then have $p_{\mathrm{T}} > 30$ GeV and pass a "medium" identification requirement. This lepton is considered isolated if it meets p_{T}- and η–dependent isolation criteria utilising calorimetric and tracking information. The criteria correspond to an efficiency of 90% (99%) for a transverse momentum of $p_{\mathrm{T}} = 25$ (60) GeV. The isolation results in an efficiency that grows as a function of the lepton p_{T}, since the background from jets misidentified as leptons becomes less important as the lepton p_{T} increases.

Jets are reconstructed from topological clusters of energy depositions [116] in the calorimeter using the anti-k_t algorithm [117], with a radius parameter value $R = 0.4$. The average energy contribution from pile-up is subtracted according to the jet area and the jets are calibrated as described in Ref [118]. They are required to have $p_T > 20$ GeV and $|\eta| < 2.5$. To reduce the effect of pile-up, a jet vertex tagger algorithm is used for jets with $p_T < 60$ GeV and $|\eta| < 2.4$. It employs a multivariate technique based on jet energy, vertexing and tracking variables to determine the likelihood that the jet originates from or is heavily contaminated by pile-up [119]. In order to identify jets containing b-hadrons (b-jets), a multivariate algorithm is used, which is based on the presence of tracks with a large impact parameter with respect to the primary vertex, the presence of displaced secondary vertices and the reconstructed flight paths of b- and c-hadrons associated with the jet [120, 121]. The algorithm has an average efficiency of 70% for b-jets and misidentification rates of approximately 8%, 1.8% and 0.26% for c-jets, hadronic tau decays and jets initiated by light quarks or gluons, respectively, as determined in simulated $t\bar{t}$ events.

Hadronic tau decays are composed of a neutrino and a set of visible decay products ($\tau_{\text{had-vis}}$), typically one or three charged pions and up to two neutral pions. The reconstruction of the visible decay products is seeded by jets [122]. The $\tau_{\text{had-vis}}$ candidates must have $p_T > 25$ (45) GeV in the $\tau_{\text{lep}}\tau_{\text{had}}$ ($\tau_{\text{had}}\tau_{\text{had}}$) channel, $|\eta| < 2.5$ excluding $1.37 < |\eta| < 1.52$, one or three associated tracks and an electric charge of ± 1. The leading-p_T $\tau_{\text{had-vis}}$ candidate in the $\tau_{\text{lep}}\tau_{\text{had}}$ channel and the two leading-p_T $\tau_{\text{had-vis}}$ candidates in the $\tau_{\text{had}}\tau_{\text{had}}$ channel are then selected and all remaining candidates are considered as jets. A Boosted Decision Tree (BDT) identification procedure, based on calorimetric shower shapes and tracking information is used to reject backgrounds from jets [123, 124]. Two $\tau_{\text{had-vis}}$ identification criteria are used: "loose" and "medium", specified in Section 5. The criteria correspond to efficiencies of about 60% (50%) and 55% (40%) in $Z/\gamma^* \rightarrow \tau\tau$ events and rejections of about 30 (30) and 50 (100) in multijet events, for one-track (three-track) $\tau_{\text{had-vis}}$ candidates, respectively. An additional dedicated likelihood-based veto is used to reduce the number of electrons misidentified as $\tau_{\text{had-vis}}$ in the $\tau_{\text{lep}}\tau_{\text{had}}$ channel, providing 95% efficiency and a background rejection between 20 and 200, depending on the pseudorapidity of the $\tau_{\text{had-vis}}$ candidate.

Geometrically overlapping objects are removed with the following priorities: (a) jets within $\Delta R = 0.2$ of selected $\tau_{\text{had-vis}}$ candidates are excluded, (b) jets within $\Delta R = 0.4$ of an electron or muon are excluded, (c) any $\tau_{\text{had-vis}}$ candidate within $\Delta R = 0.2$ of an electron or muon is excluded, (d) electrons within $\Delta R = 0.2$ of a muon are excluded.

The missing transverse momentum, with magnitude E_T^{miss}, is calculated as the modulus of the negative vectorial sum of the $\mathbf{p}_T$ of all fully reconstructed and calibrated physics objects [125, 126]. This procedure includes a "soft term", which is calculated based on the inner-detector tracks originating from the hard-scattering vertex that are not associated to reconstructed objects.

5 Event selection

5.1 $\tau_{\text{lep}}\tau_{\text{had}}$ channel

Events in the $\tau_{\text{lep}}\tau_{\text{had}}$ channel are recorded via single-electron and single-muon triggers with p_T thresholds ranging from 20 to 140 GeV and varying isolation criteria. The events must contain at least one $\tau_{\text{had-vis}}$ candidate passing the medium identification, exactly one isolated lepton (from here on referred to as ℓ) that is geometrically matched to the object that fired the trigger (implying $|\eta| < 2.4$ in the $\tau_\mu\tau_{\text{had}}$ channel), and no additional reconstructed leptons. The identified $\tau_{\text{had-vis}}$ candidate must have $|\eta| < 2.3$ to reduce

background from misidentified electrons. The isolated lepton and identified $\tau_{\text{had-vis}}$ candidate must have opposite electric charge and be back-to-back in the transverse plane: $|\Delta\phi(\ell, \tau_{\text{had-vis}})| > 2.4\,\text{rad}$, as tau leptons from the decay of heavy neutral resonances are typically produced back-to-back in the transverse plane. To reduce background from W+ jets production, the transverse mass between the isolated lepton and the missing transverse momentum, $m_{\text{T}}(\ell, E_{\text{T}}^{\text{miss}}) \equiv \sqrt{2p_{\text{T}}^{\ell} E_{\text{T}}^{\text{miss}} \left[1 - \cos\Delta\phi(\ell, E_{\text{T}}^{\text{miss}}) \right]}$, must be less than $40\,\text{GeV}$. To reduce background from $Z \to ee$ production in the $\tau_e\tau_{\text{had}}$ channel, events where the isolated lepton and identified $\tau_{\text{had-vis}}$ candidate have an invariant mass between 80 and $110\,\text{GeV}$ are rejected.

5.2 $\tau_{\text{had}}\tau_{\text{had}}$ channel

Events in the $\tau_{\text{had}}\tau_{\text{had}}$ channel are recorded using single tau triggers with p_{T} thresholds of 80, 125 or $160\,\text{GeV}$, depending on the data-taking period. Events must contain at least two $\tau_{\text{had-vis}}$ candidates with $p_{\text{T}} > 65\,\text{GeV}$ and no electrons or muons. The leading-p_{T} $\tau_{\text{had-vis}}$ candidate must be geometrically matched to the object that fired the trigger and must exceed the trigger p_{T} threshold by $5\,\text{GeV}$. The leading and sub-leading $\tau_{\text{had-vis}}$ candidates must pass the "medium" and "loose" identification criteria, respectively. They must also have opposite electric charge and be back-to-back in the transverse plane: $|\Delta\phi(\tau_1, \tau_2)| > 2.7\,\text{rad}$.

5.3 Event categories

Events satisfying the selection criteria in the $\tau_{\text{lep}}\tau_{\text{had}}$ and $\tau_{\text{had}}\tau_{\text{had}}$ channels are categorised to exploit the different production modes in the MSSM. Events containing at least one b-tagged jet enter the b-tag category, while events containing no b-tagged jets enter the b-veto category. The categorisation is not used for the Z' search.

5.4 Ditau mass reconstruction

The ditau mass reconstruction is important for achieving good separation between signal and background. However, its reconstruction is challenging due to the presence of neutrinos from the τ-lepton decays. Furthermore, the backgrounds tend to produce a higher mass along the longitudinal axis than in the transverse plane, diminishing the separation power. Therefore, the mass reconstruction used for both the $\tau_{\text{had}}\tau_{\text{had}}$ and $\tau_{\text{lep}}\tau_{\text{had}}$ channels is the total transverse mass, defined as:

$$m_{\text{T}}^{\text{tot}} \equiv \sqrt{(\mathrm{p}_{\text{T}}^{\tau_1} + p_{\text{T}}^{\tau_2} + E_{\text{T}}^{\text{miss}})^2 - (\mathbf{p}_{\text{T}}^{\tau_1} + \mathbf{p}_{\text{T}}^{\tau_2} + \mathbf{E}_{\text{T}}^{\text{miss}})^2}$$

where $\mathbf{p}_{\text{T}}^{\tau_1}$ and $\mathbf{p}_{\text{T}}^{\tau_2}$ are the momenta of the visible tau decay products (including τ_{had} and τ_{lep}) projected into the transverse plane and $\mathbf{E}_{\text{T}}^{\text{miss}}$ is the missing transverse momentum.

6 Background estimation

The dominant background contribution in the $\tau_{\text{lep}}\tau_{\text{had}}$ channel arises from processes where the $\tau_{\text{had-vis}}$ candidate originates from a quark- or gluon-initiated jet (henceforth called jet). This contribution is estimated using a data-driven fake-factor technique, described in Section 6.1. The events are divided into those where the selected lepton is correctly identified, predominantly from W+jets ($t\bar{t}$) production in the b-veto (b-tag) channel, and those where the selected lepton arises from a jet, predominantly multijet production. Backgrounds where both the $\tau_{\text{had-vis}}$ and lepton candidates originate from electrons, muons or taus (real-lepton) arise from $Z/\gamma^* \rightarrow \tau\tau$ production in the b-veto category and $t\bar{t}$ production in the b-tag category, with minor contributions from $Z/\gamma^* \rightarrow \ell\ell$, diboson and single top-quark production. These contributions are estimated using simulation. Corrections are applied to the simulation to account for mismodelling of the trigger, reconstruction, identification and isolation efficiencies, the electron to $\tau_{\text{had-vis}}$ misidentification rate and the momentum scales and resolutions. To help constrain the normalisation of the $t\bar{t}$ contribution, a control region rich in $t\bar{t}$ events is defined and included in the statistical fitting procedure. The other major background contributions can be adequately constrained in the signal regions. Events in this control region must pass the signal selection for the b-tag category, but the $m_{\text{T}}(\ell, E_{\text{T}}^{\text{miss}})$ selection is replaced by $m_{\text{T}}(\ell, E_{\text{T}}^{\text{miss}}) > 110\,(100)$ GeV in the $\tau_e\tau_{\text{had}}$ ($\tau_\mu\tau_{\text{had}}$) channel. The tighter selection in the $\tau_e\tau_{\text{had}}$ channel is used to help suppress the larger multijet contamination. The region has ~90% $t\bar{t}$ purity.

The dominant background in the $\tau_{\text{had}}\tau_{\text{had}}$ channel is multijet production, which is estimated using a fake-factor technique similar to the $\tau_{\text{lep}}\tau_{\text{had}}$ channel, described in Section 6.2. Other important background contributions come from $Z/\gamma^* \rightarrow \tau\tau$ production at high $m_{\text{T}}^{\text{tot}}$ in the b-veto category, $t\bar{t}$ production in the b-tag category, and to a lesser extent $W(\rightarrow \ell\nu)$+jets, single top-quark, diboson and $Z/\gamma^*(\rightarrow \ell\ell)$+jets production. These contributions are estimated using simulation. To improve the modelling, events in the simulation that contain jets misidentified as $\tau_{\text{had-vis}}$ candidates are weighted by fake-rates measured in W+jets and $t\bar{t}$ control regions in data.

Both channels employ fake-factor techniques that use events in control regions (CRs) where a selected $\tau_{\text{had-vis}}$ fails identification or a selected lepton fails isolation. The events are weighted by transfer-factors (fake-factors) measured in orthogonal fakes regions (FRs) to predict a given background contribution. The fake-factors are defined as the ratio of events in data which pass ($N_{\text{data}}^{\text{pass}}$) over those that fail ($N_{\text{data}}^{\text{fail}}$) a specified selection criterion. The background (N_{bkg}) is subtracted and they are parameterised against a set of auxiliary variables ($\mathbf{x}$):

$$f(\mathbf{x}) \equiv \frac{N_{\text{data}}^{\text{pass}}(\mathbf{x}) - N_{\text{bkg}}^{\text{pass}}(\mathbf{x})}{N_{\text{data}}^{\text{fail}}(\mathbf{x}) - N_{\text{bkg}}^{\text{fail}}(\mathbf{x})}\,.$$

6.1 Jet background estimate in the $\tau_{\text{lep}}\tau_{\text{had}}$ channel

Events in the $\tau_{\text{lep}}\tau_{\text{had}}$ channel where the $\tau_{\text{had-vis}}$ candidate originates from a jet are estimated using a fake-factor method to weight events in a control region which has the same selection as the signal region (SR), but where the $\tau_{\text{had-vis}}$ candidate fails identification (CR-1). The method, however, must be extended to account for the fact that multijet and W+jets (or $t\bar{t}$) events have significantly different fake-factors, which is mainly due to a different fraction of quark-initiated jets, which are typically more narrow and

produce fewer hadrons than gluon-initiated jets, and are thus more likely to pass the $\tau_{\text{had-vis}}$ identification. A schematic of the procedure is shown in Figure 2, which is described in the following.
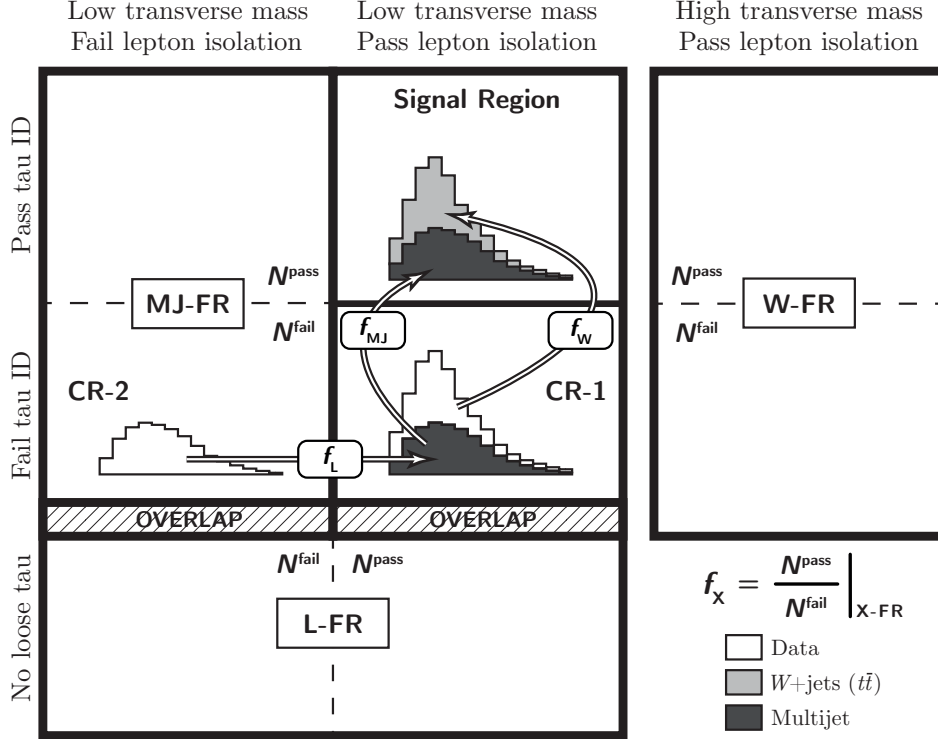

Figure 2: Schematic of the fake-factor background estimation in the $\tau_{\text{lep}}\tau_{\text{had}}$ channel. The fake-factors, f_X (X = MJ, W, L), are defined as the ratio of events in data that pass/fail the specified selection criteria, measured in the fakes-regions: MJ-FR, W-FR and L-FR, respectively. The multijet contribution is estimated by weighting events in CR-2 by the product of f_L and f_{MJ}. The contribution from W+jets and $t\bar{t}$ events where the $\tau_{\text{had-vis}}$ candidate originates from a jet is estimated by subtracting the multijet contribution from CR-1 and then weighting by f_W. There is a small overlap of events between L-FR and the CR-1 and CR-2 regions. The contribution where both the selected $\tau_{\text{had-vis}}$ and lepton originate from leptons is estimated using simulation (not shown here).

The contribution from W+jets (and $t\bar{t}$) events where the $\tau_{\text{had-vis}}$ candidate originates from a jet is estimated from events in CR-1 that remain after subtracting the multijet contribution (estimated using the technique described below) and the real-lepton contribution (estimated using simulation). The events are weighted by the W+jets tau fake-factor (f_W):

$$N^{\text{SR}}_{W+\text{jets}}(v; \mathbf{x}) = f_W(\mathbf{x}) \cdot \left[N^{\text{CR}-1}_{\text{data}}(v; \mathbf{x}) - N^{\text{CR}-1}_{\text{multijet}}(v; \mathbf{x}) - N^{\text{CR}-1}_{\text{real}-\text{lepton}}(v; \mathbf{x}) \right],$$

where v is the variable being modelled (eg. $m^{\text{tot}}_{\text{T}}$) and $\mathbf{x}$ is the set of auxiliary variables from the f_W parameterisation: $\tau_{\text{had-vis}}$ p_{T}, $\tau_{\text{had-vis}}$ track multiplicity and the azimuthal $\tau_{\text{had-vis}} - E^{\text{miss}}_{\text{T}}$ separation, $|\Delta\phi(\tau_{\text{had-vis}}, E^{\text{miss}}_{\text{T}})|$. The fake-factor f_W is measured in the W+jets fakes-region (W-FR) defined in Section 6.1.1.

The multijet contributions in both CR-1 ($N^{\text{CR}-1}_{\text{multijet}}$) and SR ($N^{\text{SR}}_{\text{multijet}}$) are estimated from events where the $\tau_{\text{had-vis}}$ fails identification and the selected lepton fails isolation (CR-2). The non-multijet background

is subtracted using simulation and the events are weighted first by the lepton-isolation fake-factor (f_{L}), yielding $N_{\text{multijet}}^{\text{CR}-1}$, and then by the multijet tau fake-factor (f_{MJ}):

$$N_{\text{multijet}}^{\text{SR}}(v; \mathbf{x}, \eta^{\ell}) = f_{\text{MJ}}(\mathbf{x}) \cdot N_{\text{multijet}}^{\text{CR}-1}(v; \mathbf{x}, \eta^{\ell}),$$

$$N_{\text{multijet}}^{\text{CR}-1}(v; \mathbf{x}, \eta^{\ell}) = f_{\text{L}}(\eta^{\ell}) \cdot \left[N_{\text{data}}^{\text{CR}-2}(v; \mathbf{x}, \eta^{\ell}) - N_{\text{non}-\text{MJ}}^{\text{CR}-2}(v; \mathbf{x}, \eta^{\ell}) \right],$$

where η^{ℓ} is the pseudorapidity of the isolated lepton, which is used to parameterise f_{L}. The fake-factor f_{MJ} is measured in the multijet fakes-region (MJ-FR) defined in Section 6.1.1 and the fake-factor f_{L} is measured in the lepton fakes-region (L-FR) defined in Section 6.1.2.

6.1.1 Tau identification fake-factors

Both f_{W} and f_{MJ} are parameterised as functions of $\tau_{\text{had-vis}}$ p_{T}, $\tau_{\text{had-vis}}$ track multiplicity and the azimuthal $\tau_{\text{had-vis}} - E_{\text{T}}^{\text{miss}}$ separation, $|\Delta\phi(\tau_{\text{had-vis}}, E_{\text{T}}^{\text{miss}})|$. The $|\Delta\phi(\tau_{\text{had-vis}}, E_{\text{T}}^{\text{miss}})|$ dependence is included to encapsulate correlations between the $\tau_{\text{had-vis}}$ identification and energy response, which impact the $E_{\text{T}}^{\text{miss}}$ calculation. Due to the limited size of the control regions, the $|\Delta\phi(\tau_{\text{had-vis}}, E_{\text{T}}^{\text{miss}})|$ dependence is extracted as a sequential correction and is only applied in the b-veto channel. The selection for W-FR and MJ-FR are the same as for SR with modifications described in the following. The $\tau_{\text{had-vis}}$ identification criterion is removed from both regions; events passing the identification enter the fake-factor numerators, while those failing enter the denominators. To reduce differences between f_{W} and f_{MJ}, a very loose $\tau_{\text{had-vis}}$ identification criterion is introduced, which tends to reject gluon-initiated jets, enhancing the fraction of quark-initiated jets. The criteria correspond to an efficiency of about 99% for $\tau_{\text{had-vis}}$ and a rejection of about 2 (3) for one-track (three-track) jets. This selection is also applied consistently to CR-1. A comparison of the two fake-factors and their respective $|\Delta\phi(\tau_{\text{had-vis}}, E_{\text{T}}^{\text{miss}})|$ corrections are shown in Figures 3(a) and 3(b).

In the W-FR, the $m_{\text{T}}(\ell, E_{\text{T}}^{\text{miss}})$ criterion is replaced by $70(60) < m_{\text{T}}(\ell, E_{\text{T}}^{\text{miss}}) < 150\,\text{GeV}$ in the $\tau_e\tau_{\text{had}}$ ($\tau_\mu\tau_{\text{had}}$) channel. The purity of $W+$ jets events that pass the $\tau_{\text{had-vis}}$ identification is ~85% in the b-veto category. The b-tag category is dominated by $t\bar{t}$ events, but the purity of events where the $\tau_{\text{had-vis}}$ candidate originates from a jet is only ~40% due to the significant $\tau_{\text{had-vis}}$ production. The multijet and real-lepton backgrounds are subtracted from W-FR analogously to CR-1 in the $W+$ jets estimate. Due to the large $\tau_{\text{had-vis}}$ contamination in the b-tag region, f_{W} is not split in category, but the b-veto parameterisation is used in the b-tag region, with a p_{T}-independent correction factor of 0.8 (0.66) for 1-prong (3-prong) $\tau_{\text{had-vis}}$. The correction factor is obtained from a direct measurement of the fake-factors in b-tag events. The subtraction of the simulated samples is affected by experimental uncertainties and uncertainties on production cross sections, which amount to 10%. The total uncertainty on the multijet estimate is also propagated to the subtraction. Due to the large contamination for b-tag events in the W-FR, a 50% uncertainty is assumed on the correction factor applied to the b-veto parameterisation. The applicability of f_{W} measured in the W-FR to CR-1 is investigated by studying f_{W} as a function of $m_{\text{T}}(\ell, E_{\text{T}}^{\text{miss}})$ and the observed differences (up to ~10%) are assigned as a systematic uncertainty. A 30% uncertainty is assigned to the sequential $|\Delta\phi(\tau_{\text{had-vis}}, E_{\text{T}}^{\text{miss}})|$ correction, based on variations observed as a function of $\tau_{\text{had-vis}}$ p_{T}.

(a) $\tau_{\text{had-vis}}$ fake-factors

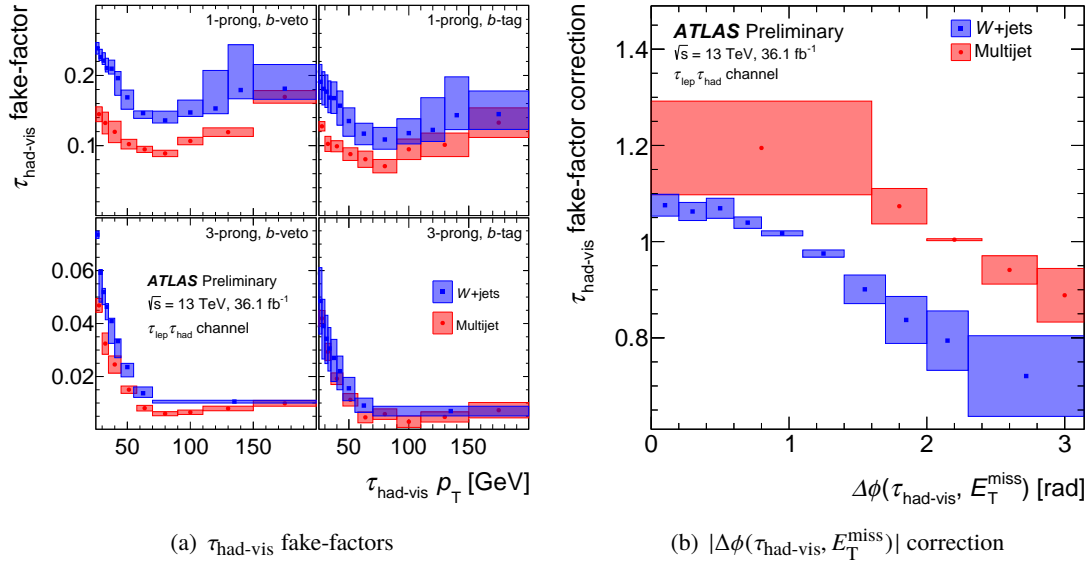(b) $|\Delta\phi(\tau_{\text{had-vis}}, E_{\text{T}}^{\text{miss}})|$ correction

Figure 3: Tau identification fake-factors and the sequential $|\Delta\phi(\tau, E_{\text{T}}^{\text{miss}})|$ correction in the $\tau_{\text{lep}}\tau_{\text{had}}$ channel. The multijet fake-factors are for the 2016 dataset only. The bands include all uncertainties.

In MJ-FR, the selected lepton must fail isolation. The multijet purity for events that pass the $\tau_{\text{had-vis}}$ identification in this region is ~88% for the b-veto category and ~93% for the b-tag category. All non-multijet contamination is subtracted from MJ-FR using simulation. The fake-factor f_{MJ} is further split by category (b-veto, b-tag) and by data-taking period (2015, 2016) to account for changing isolation criteria in the trigger that affect MJ-FR differently to SR. The applicability of f_{MJ} measured in MJ-FR to CR-1 is investigated by studying f_{MJ} as a function of the lepton isolation and the observed differences are assigned as a systematic uncertainty. The statistical uncertainty from the limited size of MJ-FR is significant, particularly for the smaller 2015 dataset. The impact of a potential mismodelling in the subtraction of simulated non-multijet events containing non-isolated leptons is investigated by varying the subtraction by 50%, but is found to be small compared to the other sources of systematic uncertainty. A constant uncertainty of 20% on f_{MJ} is used to envelope these variations. A 50% uncertainty is assigned to the sequential $|\Delta\phi(\tau_{\text{had-vis}}, E_{\text{T}}^{\text{miss}})|$ correction.

6.1.2 Lepton isolation fake-factor

The fake-factor f_{L} is measured in L-FR, which must have exactly one selected lepton, $m_{\text{T}}(\ell, E_{\text{T}}^{\text{miss}}) < 30\,\text{GeV}$ and no $\tau_{\text{had-vis}}$ candidates passing the loose identification but rather at least one selected jet (not counting the b-tagged jet in the b-tag region). The selection is designed to purify multijet events while suppressing W+jets and $t\bar{t}$ events. Events where the selected lepton passes (fails) isolation enter the f_{L} numerator (denominator). All non-multijet contributions are subtracted using simulation. The fake-factors are parameterised as a function of lepton $|\eta|$, and are further split by lepton type (electron, muon), category (b-veto, b-tag) and into two regions of muon p_{T}, due to differences in the isolation criteria of the low- and high-p_{T} triggers in the $\tau_\mu\tau_{\text{had}}$ channel. A 20% uncertainty on the background subtraction is considered, motivated by observations of the tau identification performance in W+jets events. The applicability of

12

f_{L} measured in L-FR to events in MJ-FR is investigated by altering the $m_{\text{T}}(\ell, E_{\text{T}}^{\text{miss}})$ selection and the observed differences are assigned as a systematic uncertainty. The statistical uncertainty from the limited size of L-FR is also considered, but is relatively small. The total uncertainty on f_{L} ranges from 5 to 50%.

6.2 Jet background estimate in the $\tau_{\text{had}}\tau_{\text{had}}$ channel

The fake-factor technique used to estimate the dominant multijet background in the $\tau_{\text{had}}\tau_{\text{had}}$ channel is described in Section 6.2.1. The method used to weight simulated events to estimate the remaining background containing events with $\tau_{\text{had-vis}}$ candidates that originate from jets is described in Section 6.2.2.

6.2.1 Multijet events

The contribution of multijet events in SR is estimated by weighting events in a control region that has the same selection as SR, but where the sub-leading $\tau_{\text{had-vis}}$ candidate fails identification (CR-1), by the dijet tau fake-factor (f_{DJ}), which is measured in the dijet fakes-region (DJ-FR):

$$N_{\text{multijet}}^{\text{SR}}(v; \mathbf{y}) = f_{\text{DJ}}(\mathbf{y}) \cdot \left[N_{\text{data}}^{\text{CR}-1}(v; \mathbf{y}) - N_{\text{non-MJ}}^{\text{CR}-1}(v; \mathbf{y}) \right] ,$$

where $\mathbf{y}$ is the set of auxiliary variables from the f_{DJ} parameterisation: sub-leading $\tau_{\text{had-vis}}$ p_{T} and sub-leading $\tau_{\text{had-vis}}$ track multiplicity. Unlike in the $\tau_{\text{lep}}\tau_{\text{had}}$ channel, CR-1 is completely dominated by multijet events, so a single fake-factor is sufficient. The non-multijet contamination in CR-1, $N_{\text{non-MJ}}^{\text{CR}-1}$, amounts to ~1.6% (~7.0%) in the b-veto (b-tag) channel, and is subtracted using simulation.

The selection for the DJ-FR is designed to be as similar to the signal selection as possible, while avoiding contamination from $\tau_{\text{had-vis}}$. Events are selected by single jet triggers with p_{T} thresholds ranging from 60 to 380 GeV, with all but the highest threshold trigger being prescaled. They must contain at least two $\tau_{\text{had-vis}}$ candidates, where the sub-leading candidate has $p_{\text{T}} > 65$ GeV and the leading one has $p_{\text{T}} > 85$ GeV and also exceeds the trigger threshold by 10%. The $\tau_{\text{had-vis}}$ candidates must have opposite charge sign, be back-to-back in the transverse plane, $|\Delta\phi(\tau_1, \tau_2)| > 2.7$ rad and the p_{T} of the sub-leading $\tau_{\text{had-vis}}$ must be at least 30% of the leading $\tau_{\text{had-vis}}$ p_{T}. Unlike the $\tau_{\text{lep}}\tau_{\text{had}}$ channel, the very loose $\tau_{\text{had-vis}}$ identification is not required as the background is dominated by a single process (multijet production), so there is no need to restrict the contribution from gluon-initiated jets. The fake-factors are measured using the sub-leading $\tau_{\text{had-vis}}$ candidate to avoid trigger bias and to be consistent with their application in CR-1. The purity of multijet events that pass the $\tau_{\text{had-vis}}$ identification is about 98–99% (93–98%) for the b-veto (b-tag) categories. The non-multijet contamination is subtracted using simulation. The dominant uncertainty on the fake-factors is typically due to the limited size of the DJ-FR, and ranges from 10 to 50%, however, the subtraction of the non-multijet contamination can also result in uncertainties up to 50%. An additional uncertainty is considered when applying the fake-factors in the b-tag category, which accounts for changes in the jet composition with respect to the inclusive selection of the DJ-FR. As the differences are extracted from comparisons in control regions, they are one-sided. The fake-factors are shown in Figure 4.
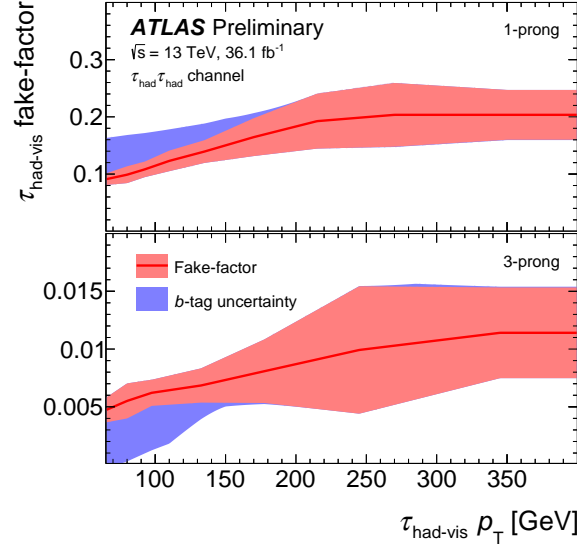
Figure 4: $\tau_{\text{had-vis}}$ identification fake-factors in the $\tau_{\text{had}}\tau_{\text{had}}$ channel. The red band indicates the total category inclusive uncertainty and the blue band indicates the additional uncertainty in the b-tag category.

6.2.2 Non-multijet events

In the $\tau_{\text{had}}\tau_{\text{had}}$ channel, backgrounds originating from jets that are misidentified as $\tau_{\text{had-vis}}$ in processes other than multijet production (predominantly W+ jets in the b-veto and $t\bar{t}$ in the b-tag categories) are estimated using simulation. Rather than applying the $\tau_{\text{had-vis}}$ identification to the simulated jets, they are weighted by fake-rates as in Ref. [46]. This not only ensures the correct fake-rate, but enhances the statistical precision of the estimate, as events failing the $\tau_{\text{had-vis}}$ identification are not discarded. The fake-rate for the sub-leading $\tau_{\text{had-vis}}$ candidate is defined as the ratio of the number of candidates that pass the identification to the total number of candidates. The fake-rate for the leading $\tau_{\text{had-vis}}$ candidate is defined as the ratio of the number of candidates that pass the identification and the single-tau trigger requirement to the total number of candidates.

The fake-rates applied to $t\bar{t}$ and single top-quark events are calculated from a control region enriched in $t\bar{t}$ events, while the fake-rates for all other processes are calculated in a control region enriched in W+ jets events. Both control regions use events selected by a single-muon trigger with a p_T threshold of 50 GeV. They must contain exactly one isolated muon with $p_T > 55$ GeV that fired the trigger, no electrons and at least one $\tau_{\text{had-vis}}$ candidate with $p_T > 50$ GeV. The events must also satisfy $|\Delta\phi(\mu, \tau_{\text{had-vis}})| > 2.4$ rad and $m_T(\mu, E_T^{\text{miss}}) > 40$ GeV. The events are then categorised into b-tag and b-veto categories, defining control regions enriched in $t\bar{t}$ and W+ jets, respectively. Backgrounds from non-$t\bar{t}$ (non-W+ jets) processes are subtracted from the $t\bar{t}$ (W+ jets) enriched control region using simulation. The fake-rates are measured using the leading-p_T $\tau_{\text{had-vis}}$ candidate and are parameterised as functions of the $\tau_{\text{had-vis}}$ p_T and track multiplicity. The uncertainty on the fake-rates is dominated by the limited size of the control regions and can reach up to 40%.

14

7 Systematic uncertainties

In this section, uncertainties affecting the simulated signal and background contributions are discussed. These include uncertainties associated with the determination of the integrated luminosity, the detector simulation, the theoretical cross sections and the modelling from the event generators. The uncertainties associated with the data-driven background estimates are discussed in Section 6.

The uncertainty in the combined 2015+2016 integrated luminosity is 3.2%, which affects all simulated samples. It is derived, following a methodology similar to that detailed in Ref. [127], from a preliminary calibration of the luminosity scale using x-y beam-separation scans performed in August 2015 and May 2016. The uncertainty related to the overlay of pile-up events is estimated by varying the average number of interactions per bunch crossing by 9%. The uncertainties related to the detector simulation manifest themselves through the efficiency of the reconstruction, identification and triggering algorithms, and the energy scale and resolution for electrons, muons, $\tau_{\text{had-vis}}$, (b-)jets and the $E_{\text{T}}^{\text{miss}}$ soft term. These uncertainties are considered for all simulated samples, and their impact is taken into account when using these samples in data-driven estimates. The effect of the particle energy scale uncertainties are propagated to the $E_{\text{T}}^{\text{miss}}$. The uncertainty on the $\tau_{\text{had-vis}}$ identification efficiency as determined from measurements of $Z \rightarrow \tau\tau$ events is 5–6%. At high p_{T}, there are no abundant sources of real hadronic tau decays from which an efficiency measurement could be made. Rather, the tau identification is studied in high-p_{T} dijet events as a function of the jet p_{T}, which indicates that there is no degradation in the modelling of the detector response as a function of the p_{T} of tau candidates. Based on the limited precision of these studies, an additional uncertainty of 20%/TeV(25%/TeV) for 1-prong (3-prong) $\tau_{\text{had-vis}}$ candidates with $p_{\text{T}} > 150\,\text{GeV}$ is assigned. The $\tau_{\text{had-vis}}$ trigger efficiency uncertainty ranges from 3 to 14%. The uncertainty on the $\tau_{\text{had-vis}}$ energy scale is 2–3%. The probability for electrons to be misidentified as $\tau_{\text{had-vis}}$ is measured with a precision of 3–14% [124]. The electron, muon, jet and $E_{\text{T}}^{\text{miss}}$ systematic uncertainties described above are found to have a very small impact.

Theoretical cross section uncertainties are taken into account for all backgrounds estimated using simulation. For Z/γ^*+jets production, uncertainties are taken from Ref. [128], which include variations of the PDF sets, scale, α_{S}, beam energy, electroweak corrections and photon-induced corrections. A single 90% CL eigenvector variation uncertainty is used, based on the CT14nnlo PDF set. The variations amount to a ~5% uncertainty on the total number of Z/γ^*+jets events within acceptance. For diboson production, an uncertainty of 5% is calculated by combining PDF, scale and α_{S} variations in quadrature. While recent improvments in the estimate of diboson cross section uncertainties [129, 130] suggest a larger value, both have a negligible impact on the analysis. For $t\bar{t}$ [103] and single top-quark [104, 105] production, a 6% uncertainty is assigned based on PDF, scale and top quark mass variations. Additional uncertainties related to initial- and final-state radiation modelling, tune and (for $t\bar{t}$ only) the choice of the `hdamp` parameter value in Powheg-Box v2, which controls the amount of radiation produced by the parton shower, are also taken into account [131]. The uncertainty on the fragmentation model is evaluated by comparing $t\bar{t}$ events generated with Powheg-Box v2 interfaced to either Herwig++ [132] or Pythia 6. To estimate the uncertainty in generating the hard scatter, the Powheg and MG5_aMC@NLO generators are compared, both interfaced to the Herwig++ parton shower model. The uncertainties on the W+jets cross section have negligible a impact in the $\tau_{\text{had}}\tau_{\text{had}}$ channel and the W+jets simulation is not used in the $\tau_{\text{lep}}\tau_{\text{had}}$ channel.

For MSSM Higgs boson samples, various sources of uncertainty are considered which impact both the production cross section and the signal acceptance. The impact from varying the factorisation and renormalisation scales up and down by a factor of two, either coherently or oppositely, is taken

15

into account. Uncertainties due to the modelling of initial- and final-state radiation, as well as multiple parton interaction are also taken into account. These uncertainties are estimated from variations of the PYTHIA 8 A14 tune [62] for the b-associated production and the AZNLO PYTHIA 8 tune [61] for the gluon fusion production. The envelope of the variations resulting from the use of the alternative PDFs in the PDF4LHC15_nlo_100 [133] set is used to estimate the PDF uncertainty for gluon fusion production. For the b-associated production, a comparison among the following PDFs is employed: NNPDF30_nlo_as_0118_nf_4 [133], CT14nlo_NF4 [59], MSTW2008nlo68cl_nf4 [134] and CT10_nlo_nf4 [58]. The total uncertainty for the MSSM Higgs boson samples ranges between 15% and 25%, which is dominated by the cross section uncertainty.

For Z' samples, uncertainties on the integrated cross section are not included in the fitting procedure used to extract experimental cross section limits. The uncertainty for Z' is included when overlaying model cross sections, in which case it is calculated using the same procedure as for the Z/γ^*+jets background.

8 Results

The number of observed events in the signal regions of the $\tau_{\mathrm{lep}}\tau_{\mathrm{had}}$ and $\tau_{\mathrm{had}}\tau_{\mathrm{had}}$ channels, along with the predicted event yields from signal and background processes, are shown in Table 1. The numbers are given before (pre-fit) and after (post-fit) applying the statistical fitting procedure described in Section 8.1. The observed event yields are compatible with the expected event yields from SM processes, within uncertainties. The $m_{\mathrm{T}}^{\mathrm{tot}}$ mass distributions are shown in Figures 5(a)–5(d).

8.1 Fit model

The parameter of interest is the signal strength, μ. It is defined as the ratio of the observed to the predicted value of the cross section times branching fraction, where the prediction is evaluated for a particular parameter space point of the theoretical model in question (MSSM or Z' benchmark scenarios). Hence, the value $\mu = 0$ corresponds to the absence of a signal, whereas the value $\mu = 1$ indicates the presence of a signal as predicted by the model. To estimate μ, a likelihood function constructed as the product of Poisson probability terms is used. A term is included for each bin in the $m_{\mathrm{T}}^{\mathrm{tot}}$ distributions from the $\tau_e\tau_{\mathrm{had}}$, $\tau_\mu\tau_{\mathrm{had}}$ and $\tau_{\mathrm{had}}\tau_{\mathrm{had}}$ channels. When fitting MSSM models to the data, the distributions are separated into b-tag and b-veto events to enhance sensitivity to the gluon fusion and b-associated production modes, while the inclusive distributions are used for Z' models. In all cases, the distributions in the top control regions of the $\tau_e\tau_{\mathrm{had}}$ and $\tau_\mu\tau_{\mathrm{had}}$ channels are added, which help constrain uncertainties on the $t\bar{t}$ background. Signal and background predictions depend on systematic uncertainties, which are parameterised as nuisance parameters that are constrained using Gaussian probability density functions. The asymptotic approximation is used with the test statistic $\tilde{q}_\mu$ [139] to compare the compatibility of the data with the null hypothesis (SM only) and with the assumed signal hypothesis (SM plus signal). The bin widths are chosen to ensure a sufficient number of background events in each bin. The results from the $\tau_e\tau_{\mathrm{had}}$, $\tau_\mu\tau_{\mathrm{had}}$ and $\tau_{\mathrm{had}}\tau_{\mathrm{had}}$ channels are combined to improve the sensitivity to signal. For ditau resonance masses below about 0.6TeV, the sensitivity is dominated by the $\tau_{\mathrm{lep}}\tau_{\mathrm{had}}$ channels, while the $\tau_{\mathrm{had}}\tau_{\mathrm{had}}$ channel is most sensitive in the higher mass range.

	b-veto		b-tag	
	$\tau_{\text{lep}}\tau_{\text{had}}$ channel			
Process	pre-fit	post-fit	pre-fit	post-fit
$Z/\gamma^* \to \tau\tau$	$92\,000 \pm 11\,000$	$95\,900 \pm 1\,700$	670 ± 140	690 ± 70
Diboson	880 ± 100	910 ± 70	6.3 ± 1.7	6.3 ± 1.3
$t\bar{t}$ and single top-quark	$1\,050 \pm 170$	$1\,080 \pm 120$	$2\,800 \pm 400$	$2\,650 \pm 80$
Jet $\to \tau$ fake	$83\,000 \pm 5\,000$	$88\,900 \pm 1\,700$	$3\,000 \pm 400$	$3\,410 \pm 170$
$Z/\gamma^* \to \ell\ell$	$15\,800 \pm 1\,200$	$16\,400 \pm 800$	86 ± 21	90 ± 16
SM Total	$193\,000 \pm 13\,000$	$203\,200 \pm 1\,200$	$6\,500 \pm 600$	$6\,840 \pm 120$
Data	203 365		6 843	
$A + H$ (300)	$1\,473 \pm 32$	–	518 ± 18	–
$A + H$ (500)	223 ± 4	–	97.6 ± 2.8	–
$A + H$ (800)	22.8 ± 0.5	–	12.6 ± 0.4	–
	$\tau_{\text{had}}\tau_{\text{had}}$ channel			
	pre-fit	post-fit	pre-fit	post-fit
Multijet	$3\,040 \pm 240$	$3\,040 \pm 90$	106 ± 32	85 ± 10
$Z/\gamma^* \to \tau\tau$	610 ± 230	730 ± 80	7.5 ± 2.9	8.0 ± 1.3
$W(\to \tau\nu)$+jets	178 ± 31	175 ± 15	4.0 ± 1.0	3.9 ± 0.5
$t\bar{t}$ and single top-quark	26 ± 9	27 ± 4	60 ± 50	69 ± 12
Others	25 ± 6	26.4 ± 2.2	1.0 ± 0.5	1.06 ± 0.35
SM Total	$3\,900 \pm 400$	$4\,000 \pm 80$	180 ± 60	167 ± 12
Data	4 059		154	
$A + H$ (300)	258 ± 8	–	96 ± 5	–
$A + H$ (500)	160.3 ± 3.0	–	70.1 ± 1.9	–
$A + H$ (800)	23.3 ± 0.4	–	13.37 ± 0.31	–

Table 1: Observed number of events and predictions of signal and background contributions in the b-veto and b-tag categories of the $\tau_{\text{lep}}\tau_{\text{had}}$ and $\tau_{\text{had}}\tau_{\text{had}}$ channels. The background predictions and uncertainties (including both statistical and systematic components) are obtained before (pre-fit) and after (post-fit) applying the statistical fitting procedure discussed in Section 8. The individual uncertainties are correlated, and do not necessarily add in quadrature to the total background uncertainty. The label "Others" refers to contributions from diboson, $Z/\gamma^*(\to \ell\ell)$+jets and $W(\to \ell\nu)$+jets production. In the $\tau_{\text{lep}}\tau_{\text{had}}$ channel, events containing a $\tau_{\text{had-vis}}$ candidate that originate from jets are removed from all processes other than Jet $\to \tau$ fake. The expected pre-fit contributions from A and H bosons with masses of 300, 500 and 800 GeV and $\tan \beta = 15$ in the hMSSM scenario are also shown.
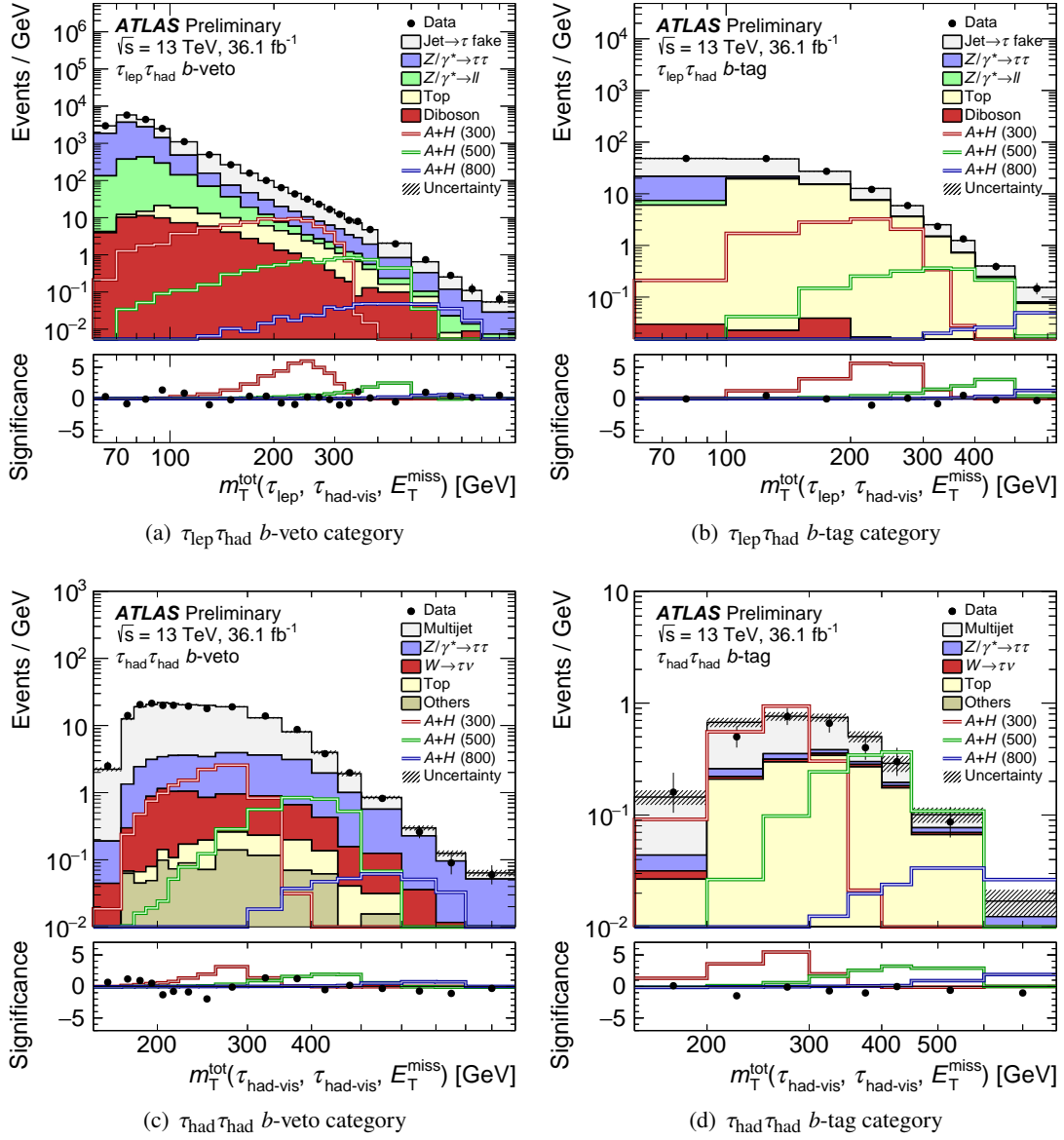
(a) $\tau_{\text{lep}}\tau_{\text{had}}$ b-veto category

(b) $\tau_{\text{lep}}\tau_{\text{had}}$ b-tag category

(c) $\tau_{\text{had}}\tau_{\text{had}}$ b-veto category

(d) $\tau_{\text{had}}\tau_{\text{had}}$ b-tag category

Figure 5: Distributions of $m_{\text{T}}^{\text{tot}}$ for the (a) b-veto and (b) b-tag, categories of the $\tau_{\text{lep}}\tau_{\text{had}}$ channel and the (c) b-veto and (d) b-tag categories of the $\tau_{\text{had}}\tau_{\text{had}}$ channel. The label "Others" refers to contributions from diboson, $Z/\gamma^*(\to \ell\ell)$+jets and $W(\to \ell\nu)$+jets production. In the $\tau_{\text{lep}}\tau_{\text{had}}$ channel, events containing $\tau_{\text{had-vis}}$ candidates that originate from jets are removed from all processes other than Jet $\to \tau$ fake. The binning displayed is that entering into the statistical fit discussed in Section 8, with minor modifications needed to combine the $\tau_{\text{lep}}\tau_{\text{had}}$ channels and with underflows and overflows included in the first and last bins, respectively. The predictions and uncertainties for the background processes are obtained from the fit under the hypothesis of no signal. The combined expectation from A and H bosons with masses of 300, 500 and 800 GeV and $\tan\beta = 15$ in the hMSSM scenario are superimposed. The significance of the data given the fitted model and its uncertainty is computed in each bin following Refs. [135–138] and is shown in the lower panels. The expected significance of the hypothetical Higgs boson signals are also overlaid.

18

8.2 Cross section limits

The data are found to be in good agreement with the predicted background yields, and the results are given in terms of exclusion limits. These are set using the modified frequentist CL_s method [140]. Upper limits on the cross section times ditau branching fraction for spin-0 (ϕ) and spin-1 (Z') bosons are set at the 95% confidence level (CL) as a function of the boson mass. They are obtained by multiplying the extracted limits on μ by the respective predicted cross sections. The spin-0 limits assume the natural width of the boson to be negligible compared to the experimental resolution (as expected over the probed MSSM parameter space). They cover the mass range 0.2–2.25 TeV and are split by production mode (gluon-fusion and b-quark associated). The limits on spin-1 bosons are calculated assuming an SSM Z' and extend up to 4 TeV. The limits are shown in Figures 6(a)–6(c). They are in the range 0.85–0.0058 pb (0.95–0.0041 pb) for gluon fusion (b-associated) production of scalar bosons with masses of 0.2–2.25 TeV and 1.56–0.0072 pb for Drell-Yan production of Z' bosons with masses of 0.2–4 TeV. A small downward fluctuation at a mass of ∼0.3 TeV is observed in all limits, while a small upward fluctuation for gluon-fusion and Z' is seen around 0.5 TeV and a broad deficit is seen for the b-quark associated production over the entire mass range. These features arise primarily because of a deficit of events in the range 200–250 GeV followed by a mild excess in the range 300–400 GeV in Figure 5(c), and by a consistent deficit of events across the whole range in Figure 5(d). Modifications of the Z' chiral coupling structure can result in changes of up to 40% in the Z' cross section limits. Reducing the Z' width can improve the limits by up to ∼30%, while increasing the width to 36% can degrade the limits by up to ∼70%. Figures 7(a) and 7(b) show the observed and expected 95% CL upper limits on the production cross section times branching fraction for $\phi \rightarrow \tau\tau$ as a function of the ratio of the gluon-fusion to b-associated production strengths and the scalar boson mass.

The impact of systematic uncertainties on the model-independent $\phi \rightarrow \tau\tau$ upper limits are calculated by comparing the expected 95% CL upper limit in case of no systematic uncertainties, μ_{stat}^{95}, with a limit calculated by introducing a group of systematic uncertainties, μ_i^{95}. The systematic impacts are shown in Figure 8(a) for gluon fusion production and Figure 8(b) for b-associated production as functions of the scalar boson mass. The major uncertainties are grouped based on their origin, while minor uncertainties are collected as "Others".

In the low mass range, the sensitivity is dominated by the $\tau_{\text{lep}}\tau_{\text{had}}$ channel, and the major uncertainties arise from the estimate of the dominant $W+$ jets background. Due to the large contribution the fit is able to significantly constrain the uncertainties on this background. In the intermediate mass range the tau energy scale and signal acceptance uncertainties become dominant. The fit is able to effectively constrain the conservative tau energy scale uncertainties due to the large contribution from $Z/\gamma^* \rightarrow \tau\tau$ and $t\bar{t}$ in each of the categories, while it is not possible to constrain the uncertainties on the signal acceptance. At very high masses, the uncertainty on the identification efficiency for high-p_{T} $\tau_{\text{had-vis}}$ candidates becomes dominant, and due to the lack of significant $Z/\gamma^* \rightarrow \tau\tau$ and $t\bar{t}$ at high mass, these uncertainties remain relatively unconstrained. The addition of the top control region distributions to the fit allows the uncertainties on the $t\bar{t}$ modelling to be well constrained and as such, they have little impact on the sensitivity.

8.3 MSSM interpretation

The data are interpreted in terms of the MSSM. Figure 9 shows regions in the m_A-tan β plane excluded at 95% CL in the $m_h^{\text{mod+}}$ and hMSSM scenarios. Constraints in the hMSSM scenario are stronger than those in the $m_h^{\text{mod+}}$ scenario due to the presence of low-mass neutralinos in the $m_h^{\text{mod+}}$ scenario that reduce the

(a) $\phi \to \tau\tau$ (gluon fusion production)

(b) $\phi \to \tau\tau$ (b-associated production)
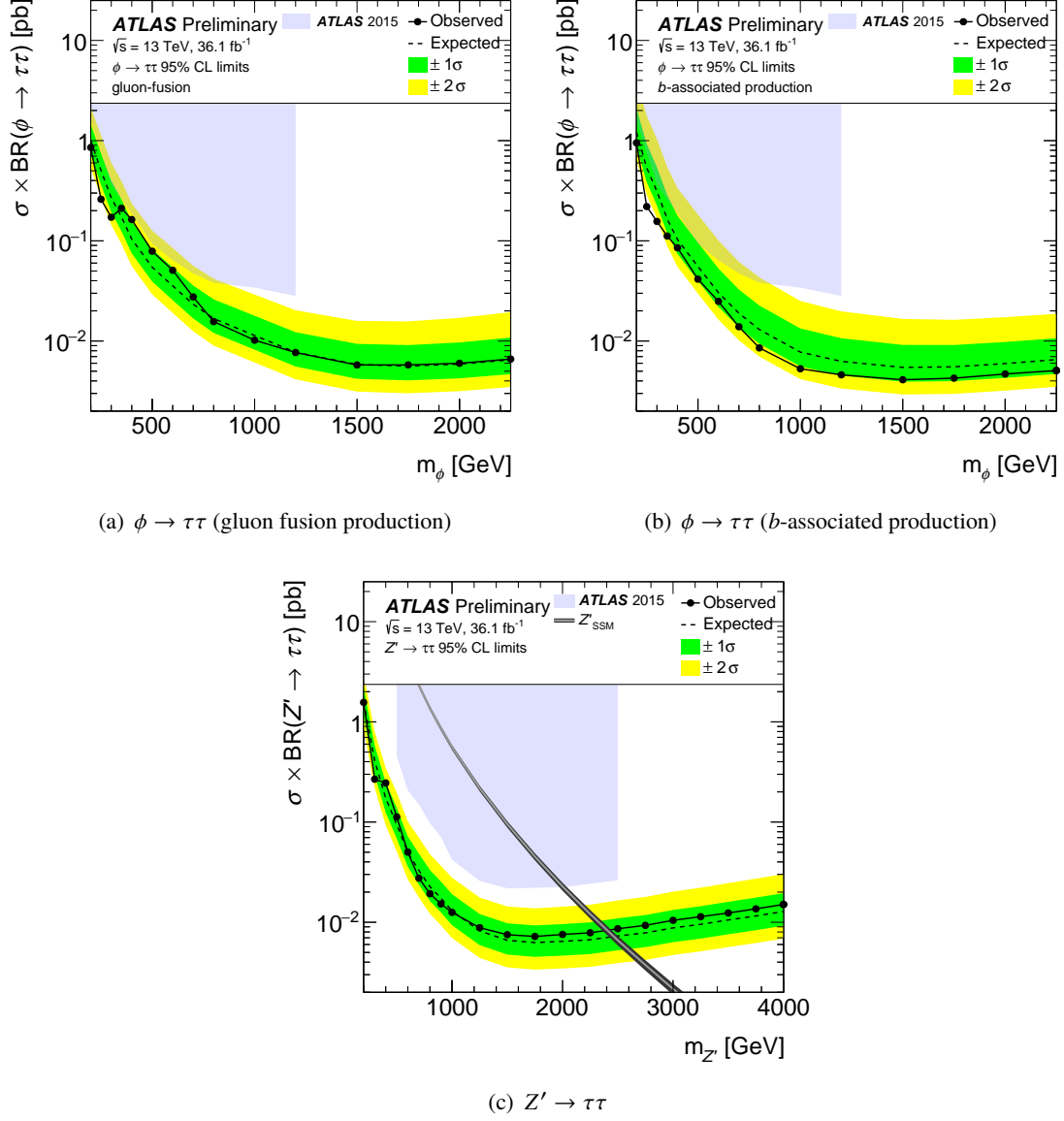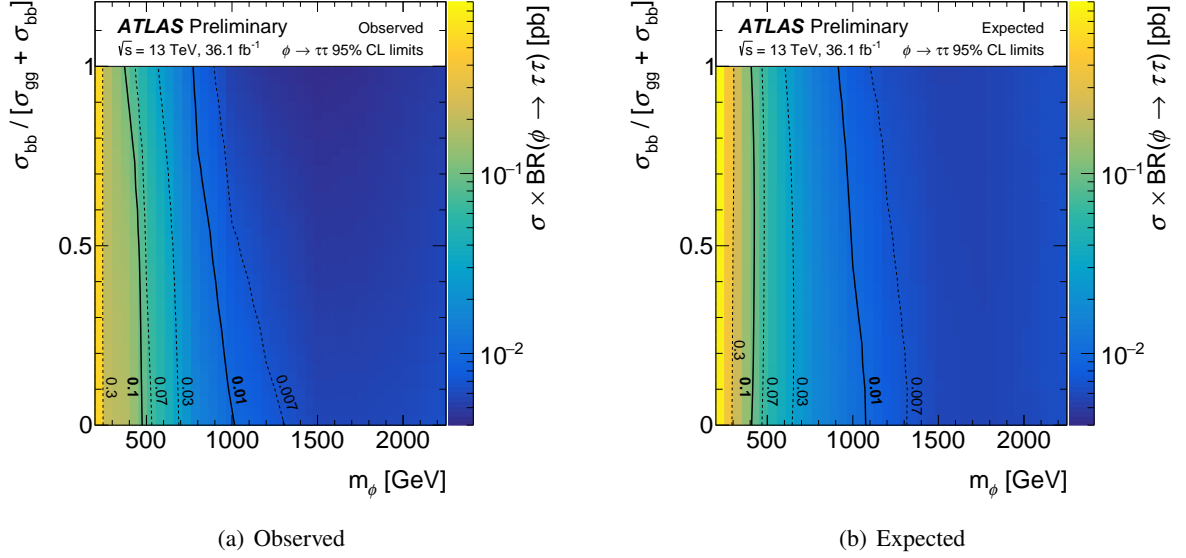

(c) $Z' \to \tau\tau$

Figure 6: The observed and expected 95% CL upper limits on the production cross section times ditau branching fraction for a scalar boson produced via (a) gluon fusion and (b) b-associated production, and for (c) gauge bosons. The limits are calculated from a statistical combination of the $\tau_{\text{lep}}\tau_{\text{had}}$ and $\tau_{\text{had}}\tau_{\text{had}}$ channels. The excluded regions from the 2015 ATLAS search [31] are depicted by the solid blue fill. The predicted cross section for a Z'_{SSM} boson is overlaid in (c), where the band depicts the total uncertainty.

(a) Observed

(b) Expected

Figure 7: The (a) observed and (b) expected 95% CL upper limit on the production cross section times branching fraction for $\phi \to \tau\tau$ as a function of the ratio of the gluon-fusion to b-associated production strengths and the scalar boson mass. The contours are overlaid.

(a) gluon fusion production

(b) b-associated production
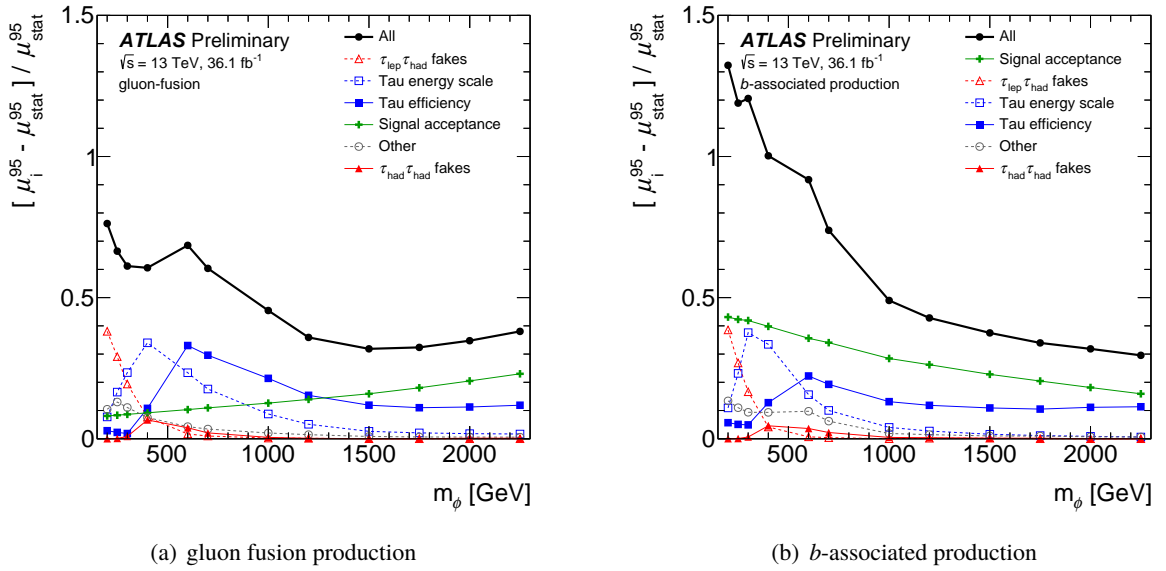
Figure 8: Impact of major groups of systematic uncertainties on the model-independent $\phi \to \tau\tau$ 95% CL upper limits on the cross section as a function of the scalar boson mass, separately for the (a) gluon fusion and (b) b-associated production mechanisms.

(a) $m_h^{\mathrm{mod+}}$ scenario   (b) hMSSM scenario
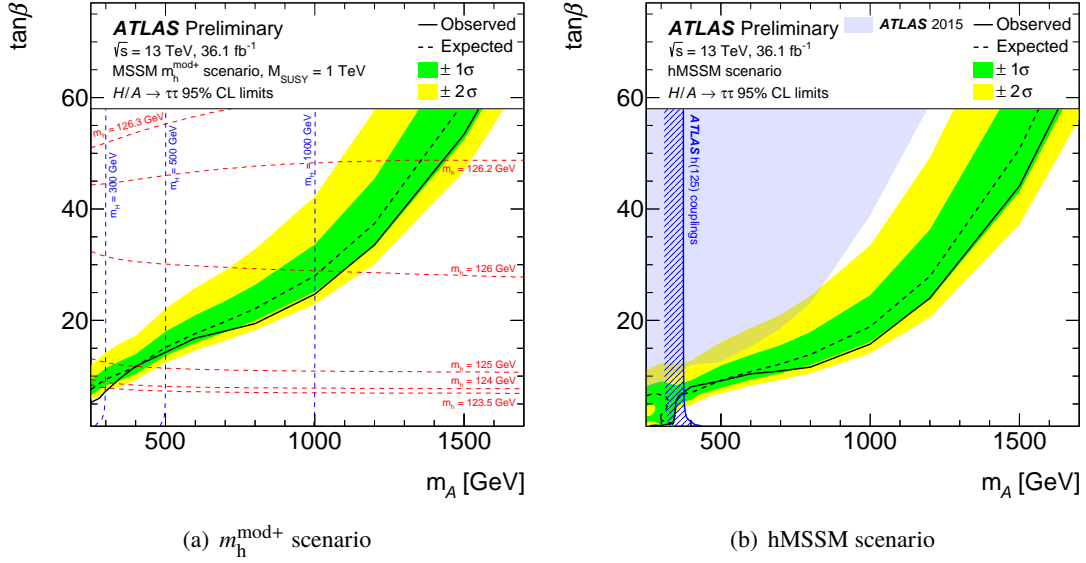
Figure 9: The observed and expected 95% CL limits on $\tan\beta$ as a function of m_A in the MSSM (a) $m_h^{\mathrm{mod+}}$ and (b) hMSSM scenarios. For the $m_h^{\mathrm{mod+}}$ scenario, dashed lines of constant m_h and m_H are shown in red and blue, respectively. For the hMSSM scenario, the exclusion arising from the SM Higgs boson coupling measurements of Ref. [141] and the exclusion limit from the ATLAS 2015 $H/A \to \tau\tau$ search result of Ref. [31] are shown.

$H/A \to \tau\tau$ branching fraction and which are absent in the hMSSM scenario. In the hMSSM scenario, the most stringent observed (expected) constraints on $\tan\beta$ for the combined search exclude $\tan\beta > 1.0$ (6.1) for $m_A = 0.25\,\mathrm{TeV}$ and $\tan\beta > 45$ (52) for $m_A = 1.5\,\mathrm{TeV}$ at 95% CL. The expected exclusion limit and bands around $m_A = 350\,\mathrm{GeV}$ reflect the behaviour of the branching ratio $A \to \tau\tau$ close to the $A \to t\bar{t}$ kinematic threshold for low $\tan\beta$, allowing for some exclusion in this region. However, when m_A is above the $A \to t\bar{t}$ production threshold, this additional decay mode reduces the sensitivity of the $A \to \tau\tau$ search for low $\tan\beta$. In the MSSM $m_h^{\mathrm{mod+}}$ scenario, the observed (expected) 95% CL upper limits exclude $\tan\beta > 5.3$ (7.5) for $m_A = 0.25\,\mathrm{TeV}$ and $\tan\beta > 54$ (60) for $m_A = 1.5\,\mathrm{TeV}$.

8.4 Z' interpretations

The data are also interpreted in terms of Z' models. As shown in Figure 6(c), the observed (expected) lower limit on the mass of a Z'_{SSM} boson is 2.42 (2.47) TeV at 95% CL. Limits at 95% CL are also placed on Z'_{SFM} bosons as a function of $m_{Z'}$ and the mixing angle between the heavy and light SU(2) gauge groups, ϕ, as shown in Figure 10. Masses below $2.25 - 2.60\,\mathrm{TeV}$ are excluded in the range $0.03 < \sin^2\phi < 0.5$ assuming no $\mu - \tau$ mixing.
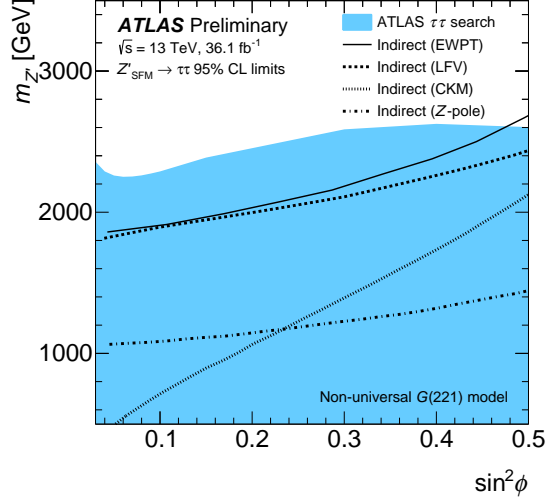
Figure 10: The 95% CL exclusion on the SFM parameter space for a $Z' \to \tau\tau$, overlaid with indirect limits at 95% CL from fits to electroweak precision measurements [142], lepton flavour violation [143], CKM unitarity [144] and Z-pole measurements [40].

9 Conclusion

A search for neutral Higgs bosons as predicted in the Minimal Supersymmetric Standard Model and Z' bosons decaying to a pair of τ-leptons is performed using a data sample from proton–proton collisions at $\sqrt{s} = 13$ TeV recorded by the ATLAS detector at the LHC, corresponding to an integrated luminosity of 36.1 fb^{-1}. The $\tau_e\tau_{\mathrm{had}}$, $\tau_\mu\tau_{\mathrm{had}}$ and $\tau_{\mathrm{had}}\tau_{\mathrm{had}}$ channels are analysed and no indication of an excess over the expected SM background is found. Upper limits on the cross section times ditau branching fraction for the production of scalar and Z' bosons are set at 95% CL, significantly increasing the sensitivity of previous searches. They are in the range 0.85–0.0058 pb (0.95–0.0041 pb) for gluon fusion (b-associated) production of scalar bosons with masses of 0.2–2.25 TeV and 1.56–0.0072 pb for Drell-Yan production of Z' bosons with masses of 0.2–4 TeV. In the context of the hMSSM scenario, the most stringent limits for the combined search exclude $\tan\beta > 1.0$ for $m_A = 0.25$ TeV and $\tan\beta > 45$ for $m_A = 1.5$ TeV at 95% CL. This analysis extends the limits set by the previous searches for the mass range $m_A > 1.2$ TeV. In the context of the Sequential Standard Model, Z'_{SSM} bosons with masses less than 2.42 TeV are excluded at 95% CL, while $m_{Z'_{\mathrm{SFM}}} < 2.25$–2.60 TeV is excluded in the range $0.03 < \sin^2\phi < 0.5$ in the Strong Flavour Model.

References

[1] ATLAS Collaboration, *Observation of a new particle in the search for the Standard Model Higgs boson with the ATLAS detector at the LHC*, Phys. Lett. B **716** (2012) 1, arXiv: 1207.7214 [hep-ex].

[2] CMS Collaboration, *Observation of a new boson at a mass of 125 GeV with the CMS experiment at the LHC*, Phys. Lett. B **716** (2012) 30, arXiv: 1207.7235 [hep-ex].

[3] L. Evans and P. Bryant, *LHC Machine*, JINST **3** (2008) S08001.

[4] ATLAS Collaboration,
Study of the spin and parity of the Higgs boson in diboson decays with the ATLAS detector,
Eur. Phys. J. C **75** (2015) 476, arXiv: 1506.05669 [hep-ex].

[5] ATLAS Collaboration, *Measurements of the Higgs boson production and decay rates and coupling strengths using pp collision data at $\sqrt{s}$ = 7 and 8 TeV in the ATLAS experiment*,
Eur. Phys. J. C **76** (2016) 6, arXiv: 1507.04548 [hep-ex].

[6] CMS Collaboration,
Precise determination of the mass of the Higgs boson and tests of compatibility of its couplings with the standard model predictions using proton collisions at 7 and 8 TeV,
Eur. Phys. J. C **75** (2015) 212, arXiv: 1412.8662 [hep-ex].

[7] CMS Collaboration, *Constraints on the spin-parity and anomalous HVV couplings of the Higgs boson in proton collisions at 7 and 8 TeV*, Phys. Rev. D **92** (2015) 012004,
arXiv: 1411.3441 [hep-ex].

[8] ATLAS and CMS Collaborations,
Measurements of the Higgs boson production and decay rates and constraints on its couplings from a combined ATLAS and CMS analysis of the LHC pp collision data at $\sqrt{s}$ = 7 and 8 TeV,
(2016), arXiv: 1606.02266 [hep-ex].

[9] F. Englert and R. Brout, *Broken symmetry and the mass of gauge vector mesons*,
Phys. Rev. Lett. **13** (1964) 321.

[10] P. W. Higgs, *Broken symmetries, massless particles and gauge fields*, Phys. Lett. **12** (1964) 132.

[11] P. W. Higgs, *Broken symmetries and the masses of gauge bosons*, Phys. Rev. Lett. **13** (1964) 508.

[12] P. W. Higgs, *Spontaneous symmetry breakdown without massless bosons*,
Phys. Rev. **145** (1966) 1156.

[13] G. Guralnik, C. Hagen and T. Kibble, *Global conservation laws and massless particles*,
Phys. Rev. Lett. **13** (1964) 585.

[14] T. Kibble, *Symmetry breaking in non-Abelian gauge theories*, Phys. Rev. **155** (1967) 1554.

[15] A. Djouadi, *The Anatomy of electro-weak symmetry breaking. II. The Higgs bosons in the minimal supersymmetric model*, Phys. Rept. **459** (2008) 1, arXiv: hep-ph/0503173.

[16] G. C. Branco et al., *Theory and phenomenology of two-Higgs-doublet models*,
Phys. Rept. **516** (2012) 1, arXiv: 1106.0034 [hep-ph].

[17] P. Fayet, *Supersymmetry and Weak, Electromagnetic and Strong Interactions*,
Phys. Lett. B **64** (1976) 159.

[18] P. Fayet, *Spontaneously Broken Supersymmetric Theories of Weak, Electromagnetic and Strong Interactions*, Phys. Lett. B **69** (1977) 489.

[19] M. Carena, S. Heinemeyer, O. Stål, C. Wagner and G. Weiglein, *MSSM Higgs Boson Searches at the LHC: Benchmark Scenarios after the Discovery of a Higgs-like Particle*,
Eur. Phys. J. C **73** (2013) 2552, arXiv: 1302.7033 [hep-ph].

[20] A. Djouadi et al., *The post-Higgs MSSM scenario: Habemus MSSM?*,
Eur. Phys. J. C **73** (2013) 2650, arXiv: 1307.5205 [hep-ph].

[21] E. Bagnaschi et al., *Benchmark scenarios for low* tan β *in the MSSM*, LHCHXSWG-2015-002, 2015, URL: http://cdsweb.cern.ch/record/2039911.

[22] ALEPH, DELPHI, L3, and OPAL Collaborations, G. Abbiendi et al., *Search for neutral MSSM Higgs bosons at LEP*, Eur. Phys. J. C **47** (2006) 547, arXiv: hep-ex/0602042 [hep-ex].

[23] Tevatron New Phenomena & Higgs Working Group Collaboration, B. Doug et al., *Combined CDF and D0 upper limits on MSSM Higgs boson production in* $\tau\tau$ *final states with up to* 2.2 fb^{-1}, (2010), arXiv: 1003.3363 [hep-ex].

[24] CDF Collaboration, T. Aaltonen et al., *Search for Higgs bosons predicted in two-Higgs-doublet models via decays to* τ *lepton pairs in 1.96 TeV proton–antiproton collisions*, Phys. Rev. Lett. **103** (2009) 201801, arXiv: 0906.1014 [hep-ex].

[25] D0 Collaboration, V. M. Abazov et al., *Search for Higgs bosons decaying to* τ *pairs in* $p\bar{p}$ *collisions with the D0 detector*, Phys. Rev. Lett. **101** (2008) 071804, arXiv: 0805.2491 [hep-ex].

[26] ATLAS Collaboration, *Search for the neutral Higgs bosons of the minimal supersymmetric standard model in pp collisions at* $\sqrt{s} = 7$ *TeV with the ATLAS detector*, JHEP **02** (2013) 095, arXiv: 1211.6956 [hep-ex].

[27] ATLAS Collaboration, *Search for neutral Higgs bosons of the minimal supersymmetric standard model in pp collisions at* $\sqrt{s} = 8$ *TeV with the ATLAS detector*, JHEP **11** (2014) 056, arXiv: 1409.6064 [hep-ex].

[28] CMS Collaboration, *Search for neutral MSSM Higgs bosons decaying to a pair of tau leptons in pp collisions*, JHEP **10** (2014) 160, arXiv: 1408.3316 [hep-ex].

[29] CMS Collaboration, *Search for Neutral MSSM Higgs Bosons Decaying into A Pair of Bottom Quarks*, JHEP **11** (2015) 071, arXiv: 1506.08329 [hep-ex].

[30] LHCb Collaboration, R. Aaij et al., *Limits on neutral Higgs boson production in the forward region in pp collisions at* $\sqrt{s} = 7$ *TeV*, JHEP **05** (2013) 132, arXiv: 1304.2591 [hep-ex].

[31] ATLAS Collaboration, *Search for Minimal Supersymmetric Standard Model Higgs bosons H/A and for a Z′ boson in the* $\tau\tau$ *final state produced in pp collisions at* $\sqrt{s} = 13$ *TeV with the ATLAS Detector*, Eur. Phys. J. C **76** (2016) 585, arXiv: 1608.00890 [hep-ex].

[32] CMS Collaboration, *Search for a neutral MSSM Higgs boson decaying into* $\tau\tau$ *at 13 TeV*, CMS-PAS-HIG-16-006, 2016, URL: http://cds.cern.ch/record/2160252.

[33] J. L. Hewett and T. G. Rizzo, *Low-energy phenomenology of superstring-inspired* E_6 *models*, Phys. Rept. **183** (1989) 193.

[34] M. Cvetic and S. Godfrey, *Discovery and identification of extra gauge bosons*, (1995), arXiv: hep-ph/9504216.

[35] A. Leike, *The Phenomenology of extra neutral gauge bosons*, Phys. Rept. **317** (1999) 143, arXiv: hep-ph/9805494.

[36] R. Diener, S. Godfrey and T. A. Martin,
Unravelling an Extra Neutral Gauge Boson at the LHC using Third Generation Fermions,
Phys. Rev. D **83** (2011) 115008, arXiv: `1006.2845 [hep-ph]`.

[37] P. Langacker, *The Physics of Heavy Z′ Gauge Bosons*, Rev. Mod. Phys. **81** (2009) 1199,
arXiv: `0801.1345 [hep-ph]`.

[38] G. Altarelli, B. Mele and M. Ruiz-Altaba,
Searching for New Heavy Vector Bosons in $p\bar{p}$ Colliders,
Z. Phys. **C45** (1989) 109, [Erratum: Z. Phys.C47,676(1990)].

[39] K. R. Lynch, E. H. Simmons, M. Narain and S. Mrenna,
Finding Z′ bosons coupled preferentially to the third family at LEP and the Tevatron,
Phys. Rev. D **63** (2001) 035006, arXiv: `hep-ph/0007286`.

[40] E. Malkawi, T. Tait and C.-P. Yuan, *A model of strong flavor dynamics for the top quark*,
Phys. Lett. B **385** (1996) 304, arXiv: `hep-ph/9603349`.

[41] K. Hsieh, K. Schmitz, J.-H. Yu and C.-P. Yuan,
Global analysis of general $SU(2) \times SU(2) \times U(1)$ models with precision data,
Phys. Rev. D **82** (2010) 035011, arXiv: `1003.3482 [hep-ph]`.

[42] D. J. Muller and S. Nandi, *Top flavor: A Separate SU(2) for the third family*,
Phys. Lett. B **383** (1996) 345, arXiv: `hep-ph/9602390`.

[43] R. S. Chivukula and E. H. Simmons, *Electroweak limits on nonuniversal Z′ bosons*,
Phys. Rev. D **66** (2002) 015006, arXiv: `hep-ph/0205064`.

[44] ATLAS Collaboration, *A search for high-mass resonances decaying to tau+tau- in pp collisions
at $\sqrt{s}$ = 7 TeV with the ATLAS detector*, Phys. Lett. B **719** (2013) 242,
arXiv: `1210.6604 [hep-ex]`.

[45] CMS Collaboration,
Search for high-mass resonances decaying into tau-lepton pairs in pp collisions at $\sqrt{s}$ = 7 TeV,
Phys. Lett. B **716** (2012) 82, arXiv: `1206.1725 [hep-ex]`.

[46] ATLAS Collaboration, *A search for high-mass resonances decaying to $\tau^+\tau^-$ in pp collisions at
$\sqrt{s}$ = 8 TeV with the ATLAS detector*, JHEP **07** (2015) 157, arXiv: `1502.07177 [hep-ex]`.

[47] ATLAS Collaboration, *The ATLAS experiment at the CERN Large Hadron Collider*,
JINST **3** (2008) S08003.

[48] ATLAS Collaboration, *ATLAS insertable B-layer technical design report*, ATLAS-TDR-19,
2010, URL: `http://cds.cern.ch/record/1291633`.

[49] ATLAS Collaboration, *ATLAS insertable B-layer technical design report addendum*,
ATLAS-TDR-19-ADD-1, 2012, URL: `http://cds.cern.ch/record/1451888`.

[50] ATLAS Collaboration, *Performance of the ATLAS Trigger System in 2015*,
Eur. Phys. J. **C77** (2017) 317, arXiv: `1611.09661 [hep-ex]`.

[51] ATLAS Collaboration, *Trigger Menu in 2016*, ATL-DAQ-PUB-2017-001, 2017,
URL: `https://cds.cern.ch/record/2242069`.

[52] ATLAS Collaboration,
Selection of jets produced in 13 TeV proton–proton collisions with the ATLAS detector,
ATLAS-CONF-2015-029, 2015, URL: `https://cds.cern.ch/record/2037702`.

[53] P. Nason, *A New method for combining NLO QCD with shower Monte Carlo algorithms*, JHEP **11** (2004) 040, arXiv: `hep-ph/0409146`.

[54] S. Frixione, P. Nason and C. Oleari, *Matching NLO QCD computations with Parton Shower simulations: the POWHEG method*, JHEP **11** (2007) 070, arXiv: `0709.2092 [hep-ph]`.

[55] S. Alioli, P. Nason, C. Oleari and E. Re, *A general framework for implementing NLO calculations in shower Monte Carlo programs: the POWHEG BOX*, JHEP **06** (2010) 043, arXiv: `1002.2581 [hep-ph]`.

[56] J. Alwall, R. Frederix, S. Frixione, V. Hirschi, F. Maltoni et al., *The automated computation of tree-level and next-to-leading order differential cross sections, and their matching to parton shower simulations*, JHEP **07** (2014) 079, arXiv: `1405.0301 [hep-ph]`.

[57] M. Wiesemann et al., *Higgs production in association with bottom quarks*, JHEP **02** (2015) 132, arXiv: `1409.5301 [hep-ph]`.

[58] H.-L. Lai et al., *New parton distributions for collider physics*, Phys. Rev. D **82** (2010) 074024, arXiv: `1007.2241 [hep-ph]`.

[59] S. Dulat et al., *New parton distribution functions from a global analysis of quantum chromodynamics*, Phys. Rev. D **93** (2016) 033006, arXiv: `1506.07443 [hep-ph]`.

[60] T. Sjöstrand et al., *An Introduction to PYTHIA 8.2*, Comput. Phys. Commun. **191** (2015) 159, arXiv: `1410.3012 [hep-ph]`.

[61] ATLAS Collaboration, *Measurement of the Z/γ^* boson transverse momentum distribution in pp collisions at $\sqrt{s}$ = 7 TeV with the ATLAS detector*, JHEP **09** (2014) 55, arXiv: `1406.3660 [hep-ex]`.

[62] ATLAS Collaboration, *ATLAS Pythia 8 tunes to 7 TeV data*, ATL-PHYS-PUB-2014-021, 2014, URL: `https://cds.cern.ch/record/1966419`.

[63] J. Pumplin, D. Stump, J. Huston, H. Lai, P. M. Nadolsky et al., *New generation of parton distributions with uncertainties from global QCD analysis*, JHEP **07** (2002) 012, arXiv: `hep-ph/0201195`.

[64] R. D. Ball et al., *Parton distributions with LHC data*, Nucl. Phys. B **867** (2013) 244, arXiv: `1207.1303 [hep-ph]`.

[65] LHC Higgs Cross Section Working Group, *Handbook of LHC Higgs Cross Sections: 4. Deciphering the Nature of the Higgs Sector*, (2016), arXiv: `1610.07922 [hep-ph]`.

[66] R. V. Harlander, S. Liebler and H. Mantler, *SusHi: A program for the calculation of Higgs production in gluon fusion and bottom-quark annihilation in the Standard Model and the MSSM*, Comp. Phys. Commun. **184** (2013) 1605, arXiv: `1212.3249 [hep-ph]`.

[67] M. Spira, A. Djouadi, D. Graudenz and P. M. Zerwas, *Higgs boson production at the LHC*, Nucl. Phys. B **453** (1995) 17, arXiv: `hep-ph/9504378`.

[68] U. Aglietti, R. Bonciani, G. Degrassi and A. Vicini, *Two loop light fermion contribution to Higgs production and decays*, Phys. Lett. B **595** (2004) 432, arXiv: `hep-ph/0404071`.

27

[69] R. Harlander and P. Kant,
Higgs production and decay: Analytic results at next-to-leading order QCD,
JHEP **12** (2005) 015, arXiv: `hep-ph/0509189`.

[70] R. Bonciani, G. Degrassi and A. Vicini,
On the Generalized Harmonic Polylogarithms of One Complex Variable,
Comput. Phys. Commun. **182** (2011) 1253, arXiv: `1007.1891 [hep-ph]`.

[71] G. Degrassi, S. Di Vita and P. Slavich, *On the NLO QCD Corrections to the Production of the Heaviest Neutral Higgs Scalar in the MSSM*, Eur. Phys. J. C **72** (2012) 2032,
arXiv: `1204.1016 [hep-ph]`.

[72] R. Harlander and W. B. Kilgore,
Higgs boson production in bottom quark fusion at next-to-next-to-leading order,
Phys. Rev. D **68** (2003) 013001, arXiv: `hep-ph/0304035`.

[73] S. Dittmaier, M. Krämer and M. Spira,
Higgs radiation off bottom quarks at the Tevatron and the LHC, Phys. Rev. D **70** (2004) 074010,
arXiv: `hep-ph/0309204`.

[74] S. Dawson, C. B. Jackson, L. Reina and D. Wackeroth,
Exclusive Higgs boson production with bottom quarks at hadron colliders,
Phys. Rev. D **69** (2004) 074027, arXiv: `hep-ph/0311067`.

[75] R. Harlander, M. Krämer and M. Schumacher, *Bottom-quark associated Higgs-boson production: reconciling the four- and five-flavour scheme approach*, (2011),
arXiv: `1112.3478 [hep-ph]`.

[76] S. Heinemeyer, W. Hollik and G. Weiglein, *FeynHiggs: A Program for the calculation of the masses of the neutral CP even Higgs bosons in the MSSM*,
Comput. Phys. Commun. **124** (2000) 76, arXiv: `hep-ph/9812320`.

[77] S. Heinemeyer, W. Hollik and G. Weiglein, *The Masses of the neutral CP - even Higgs bosons in the MSSM: Accurate analysis at the two loop level*, Eur. Phys. J. C **9** (1999) 343,
arXiv: `hep-ph/9812472`.

[78] G. Degrassi, S. Heinemeyer, W. Hollik, P. Slavich and G. Weiglein,
Towards high precision predictions for the MSSM Higgs sector, Eur. Phys. J. C **28** (2003) 133,
arXiv: `hep-ph/0212020`.

[79] T. Hahn, S. Heinemeyer, W. Hollik, H. Rzehak and G. Weiglein, *High-Precision Predictions for the Light CP -Even Higgs Boson Mass of the Minimal Supersymmetric Standard Model*,
Phys. Rev. Lett. **112** (2014) 141801, arXiv: `1312.4937 [hep-ph]`.

[80] LHC Higgs Cross Section Working Group,
Handbook of LHC Higgs Cross Sections: 3. Higgs Properties, (2013),
arXiv: `1307.1347 [hep-ph]`.

[81] A. Djouadi, J. Kalinowski and M. Spira, *HDECAY: A Program for Higgs boson decays in the standard model and its supersymmetric extension*, Comput. Phys. Commun. **108** (1998) 56,
arXiv: `hep-ph/9704448`.

[82] Z. Czyczula, T. Przedzinski and Z. Was,
TauSpinner Program for Studies on Spin Effect in tau Production at the LHC,
Eur. Phys. J. C **72** (2012) 1988, arXiv: `1201.0117 [hep-ph]`.

[83] A. Kaczmarska, J. Piatlicki, T. Przedzinski, E. Richter-Was and Z. Was,
Application of TauSpinner for Studies on τ-Lepton Polarization and Spin Correlations in Z, W and H Decays at the LHC, Acta Phys. Polon. B **45** (2014) 1921, arXiv: 1402.2068 [hep-ph].

[84] S. Banerjee, J. Kalinowski, W. Kotlarski, T. Przedzinski and Z. Was,
Ascertaining the spin for new resonances decaying into tau+ tau- at Hadron Colliders,
Eur. Phys. J. C **73** (2013) 2313, arXiv: 1212.2873 [hep-ph].

[85] T. Sjöstrand, S. Mrenna and P. Skands, *A Brief Introduction to PYTHIA 8.1*,
Comput. Phys. Commun. **178** (2008) 852, arXiv: 0710.3820 [hep-ph].

[86] T. Sjöstrand, S. Mrenna and P. Skands, *PYTHIA 6.4 physics and manual*, JHEP **05** (2006) 026,
arXiv: hep-ph/0603175.

[87] C. Anastasiou, L. J. Dixon, K. Melnikov and F. Petriello, *High precision QCD at hadron colliders: Electroweak gauge boson rapidity distributions at NNLO*,
Phys. Rev. D **69** (2004) 094008, arXiv: hep-ph/0312266.

[88] S. Alioli, P. Nason, C. Oleari and E. Re,
NLO Higgs boson production via gluon fusion matched with shower in POWHEG,
JHEP **04** (2009) 002, arXiv: 0812.0578 [hep-ph].

[89] D. J. Lange, *The EvtGen particle decay simulation package*,
Nucl. Instrum. Meth. A **462** (2001) 152.

[90] N. Davidson, T. Przedzinski and Z. Was,
PHOTOS Interface in C++: Technical and Physics Documentation,
Comput. Phys. Commun. **199** (2016) 86, arXiv: 1011.0937 [hep-ph].

[91] S. G. Bondarenko and A. A. Sapronov,
NLO EW and QCD proton-proton cross section calculations with mcsanc-v1.01,
Comput. Phys. Commun. **184** (2013) 2343, arXiv: 1301.3687 [hep-ph].

[92] A. D. Martin, R. G. Roberts, W. J. Stirling and R. S. Thorne,
Parton distributions incorporating QED contributions, Eur. Phys. J. **C39** (2005) 155,
arXiv: hep-ph/0411040 [hep-ph].

[93] T. Gleisberg et al., *Event generation with SHERPA 1.1*, JHEP **02** (2009) 007,
arXiv: 0811.4622 [hep-ph].

[94] T. Gleisberg and S. Höche, *Comix, a new matrix element generator*, JHEP **12** (2008) 039,
arXiv: 0808.3674 [hep-ph].

[95] F. Cascioli, P. Maierhofer and S. Pozzorini, *Scattering Amplitudes with Open Loops*,
Phys. Rev. Lett. **108** (2012) 111601, arXiv: 1111.5206 [hep-ph].

[96] S. Schumann and F. Krauss,
A Parton shower algorithm based on Catani-Seymour dipole factorisation, JHEP **03** (2008) 038,
arXiv: 0709.1027 [hep-ph].

[97] S. Höche, F. Krauss, M. Schönherr and F. Siegert,
QCD matrix elements + parton showers: The NLO case, JHEP **04** (2013) 027,
arXiv: 1207.5030 [hep-ph].

[98] C. Anastasiou, L. J. Dixon, K. Melnikov and F. Petriello, *High precision QCD at hadron colliders: Electroweak gauge boson rapidity distributions at NNLO*,
Phys. Rev. D **69** (2004) 094008, arXiv: hep-ph/0312266.

[99] K. Melnikov and F. Petriello,
*Electroweak gauge boson production at hadron colliders through O(alpha(s)**2)*,
Phys. Rev. D **74** (2006) 114017, arXiv: hep-ph/0609070.

[100] R. Gavin, Y. Li, F. Petriello and S. Quackenbush,
FEWZ 2.0: A code for hadronic Z production at next-to-next-to-leading order,
Comput. Phys. Commun. **182** (2011) 2388, arXiv: 1011.3540 [hep-ph].

[101] P. Artoisenet, R. Frederix, O. Mattelaer and R. Rietkerk,
Automatic spin-entangled decays of heavy resonances in Monte Carlo simulations,
JHEP **03** (2013) 015, arXiv: 1212.3460 [hep-ph].

[102] P. Skands, *Tuning Monte Carlo Generators: The Perugia Tunes*, Phys. Rev. D **82** (2010) 074018,
arXiv: 1005.3457 [hep-ph].

[103] M. Czakon and A. Mitov,
Top++: A Program for the Calculation of the Top-Pair Cross-Section at Hadron Colliders,
Comput. Phys. Commun. **185** (2014) 2930, arXiv: 1112.5675 [hep-ph].

[104] P. Kant et al., *HatHor for single top-quark production: Updated predictions and uncertainty
estimates for single top-quark production in hadronic collisions*,
Comput. Phys. Commun. **191** (2015) 74, arXiv: 1406.4403 [hep-ph].

[105] M. Aliev, H. Lacker, U. Langenfeld, S. Moch, P. Uwer et al.,
HatHor: HAdronic Top and Heavy quarks crOss section calculatoR,
Comput. Phys. Commun. **182** (2011) 1034, arXiv: 1007.1327 [hep-ph].

[106] N. Kidonakis,
Two-loop soft anomalous dimensions for single top quark associated production with a W- or H-,
Phys. Rev. D **82** (2010) 054018, arXiv: 1005.4451 [hep-ph].

[107] ATLAS Collaboration, *Summary of ATLAS Pythia 8 tunes*, ATL-PHYS-PUB-2012-003, 2012,
URL: http://cdsweb.cern.ch/record/1474107.

[108] A. D. Martin et al., *Parton distributions for the LHC*, Eur. Phys. J. C **63** (2009) 189,
arXiv: 0901.0002 [hep-ph].

[109] S. Agostinelli et al., GEANT4 Collaboration, *GEANT4 - a simulation toolkit*,
Nucl. Instrum. Meth. A **506** (2003) 250.

[110] ATLAS Collaboration, *The ATLAS simulation infrastructure*, Eur. Phys. J. C **70** (2010) 823,
arXiv: 1005.4568 [physics.ins-det].

[111] ATLAS Collaboration, *The simulation principle and performance of the ATLAS fast calorimeter
simulation FastCaloSim*, ATL-PHYS-PUB-2010-013, 2010,
URL: http://cdsweb.cern.ch/record/1300517.

[112] ATLAS Collaboration, *Electron reconstruction and identification efficiency measurements with
the ATLAS detector using the 2011 LHC proton–proton collision data*,
Eur. Phys. J. C **74** (2014) 2941, arXiv: 1404.2240 [hep-ex].

[113] ATLAS Collaboration,
Electron and photon energy calibration with the ATLAS detector using LHC Run 1 data,
Eur. Phys. J. C **74** (2014) 3071, arXiv: 1407.5063 [hep-ex].

[114] ATLAS Collaboration, *Electron identification measurements in ATLAS using $\sqrt{s}$ = 13 TeV data
with* 50 *ns bunch spacing*, ATL-PHYS-PUB-2015-041, 2015,
URL: https://cds.cern.ch/record/2048202.

[115] ATLAS Collaboration, *Muon reconstruction performance of the ATLAS detector in proton–proton collision data at $\sqrt{s}$ = 13 TeV*, Eur. Phys. J. C **76** (2016) 292, arXiv: 1603.05598 [hep-ex].

[116] ATLAS Collaboration, *Topological cell clustering in the ATLAS calorimeters and its performance in LHC Run 1*, (2016), arXiv: 1603.02934 [hep-ex].

[117] M. Cacciari, G. P. Salam and G. Soyez, *The anti-k_t jet clustering algorithm*, JHEP **04** (2008) 063, arXiv: 0802.1189 [hep-ph].

[118] ATLAS Collaboration, *Jet energy scale measurements and their systematic uncertainties in proton–proton collisions at $\sqrt{s}$ = 13 TeV with the ATLAS detector*, (2017), arXiv: 1703.09665 [hep-ex].

[119] ATLAS Collaboration, *Performance of pile-up mitigation techniques for jets in pp collisions at $\sqrt{s}$ = 8 TeV using the ATLAS detector*, Eur. Phys. J. C **76** (2016) 581, arXiv: 1510.03823 [hep-ex].

[120] ATLAS Collaboration, *Performance of b-Jet Identification in the ATLAS Experiment*, JINST **11** (2016) P04008, arXiv: 1512.01094 [hep-ex].

[121] ATLAS Collaboration, *Optimisation of the ATLAS b-tagging performance for the 2016 LHC Run*, ATL-PHYS-PUB-2016-012, 2016, URL: https://cds.cern.ch/record/2160731.

[122] ATLAS Collaboration, *Identification and energy calibration of hadronically decaying tau leptons with the ATLAS experiment in pp collisions at $\sqrt{s}$ = 8 TeV*, Eur. Phys. J. C **75** (2015) 303, arXiv: 1412.7086 [hep-ex].

[123] ATLAS Collaboration, *Reconstruction, Energy Calibration, and Identification of Hadronically Decaying Tau Leptons in the ATLAS Experiment for Run-2 of the LHC*, ATL-PHYS-PUB-2015-045, 2015, URL: https://cds.cern.ch/record/2064383.

[124] ATLAS Collaboration, *Measurement of the tau lepton reconstruction and identification performance in the ATLAS experiment using pp collisions at $\sqrt{s}$ = 13 TeV*, ATLAS-CONF-2017-029, 2017, URL: https://cds.cern.ch/record/2261772.

[125] ATLAS Collaboration, *Performance of missing transverse momentum reconstruction with the ATLAS detector in the first proton–proton collisions at $\sqrt{s}$ = 13 TeV*, ATL-PHYS-PUB-2015-027, 2015, URL: https://cds.cern.ch/record/2037904.

[126] ATLAS Collaboration, *Expected performance of missing transverse momentum reconstruction for the ATLAS detector at $\sqrt{s}$ = 13 TeV*, ATL-PHYS-PUB-2015-023, 2015, URL: https://cds.cern.ch/record/2037700.

[127] ATLAS Collaboration, *Luminosity determination in pp collisions at $\sqrt{s}$ = 8 TeV using the ATLAS detector at the LHC*, Eur. Phys. J. C **76** (2016) 653, arXiv: 1608.03953 [hep-ex].

[128] ATLAS Collaboration, *Search for high-mass new phenomena in the dilepton final state using proton–proton collisions at $\sqrt{s}$ = 13 TeV with the ATLAS detector*, Phys. Lett. B **761** (2016) 372, arXiv: 1607.03669 [hep-ex].

[129] J. M. Campbell, R. K. Ellis and C. Williams, *Vector boson pair production at the LHC*, JHEP **07** (2011) 018, arXiv: 1105.0020 [hep-ph].

[130] T. Gleisberg, S. Höche, F. Krauss, M. Schönherr, S. Schumann et al.,
Event generation with SHERPA 1.1, JHEP **02** (2009) 007, arXiv: `0811.4622 [hep-ph]`.

[131] ATLAS Collaboration,
Simulation of top-quark production for the ATLAS experiment at $\sqrt{s}$ = 13 TeV,
ATL-PHYS-PUB-2016-004, 2016, URL: `http://cdsweb.cern.ch/record/2120417`.

[132] M. Bahr et al., *Herwig++ Physics and Manual*, Eur. Phys. J. C **58** (2008) 639,
arXiv: `0803.0883 [hep-ph]`.

[133] R. D. Ball et al., *Parton distributions for the LHC Run II*, JHEP **04** (2015) 040,
arXiv: `1410.8849 [hep-ph]`.

[134] A. Martin, W. J. Stirling, R. S. Thorne and G. Watt,
Heavy-quark mass dependence in global PDF analyses and 3- and 4-flavour parton distributions,
Eur. Phys. J. C **70** (2010) 51, arXiv: `1007.2624 [hep-ph]`.

[135] R. D. Cousins, *"RooStats::NumberCountingUtils"*,
URL: `https://root.cern.ch/root/html526/RooStats__NumberCountingUtils.html`.

[136] R. D. Cousins, J. T. Linnemann and J. Tucker,
*Evaluation of three methods for calculating statistical significance when incorporating a
systematic uncertainty into a test of the background-only hypothesis for a Poisson process*,
Nucl. Instr. Meth. Phys. Res. A **595** (2008) 480, arXiv: `physics/0702156`.

[137] K. Cranmer, *Statistical Challenges for Searches for New Physics at the LHC*, (2006),
arXiv: `physics/0511028`.

[138] J. Linnemann, *Measures of Significance in HEP and Astrophysics*, (2003),
arXiv: `physics/0312059`.

[139] G. Cowan, K. Cranmer, E. Gross and O. Vitells,
Asymptotic formulae for likelihood-based tests of new physics,
Eur. Phys. J. C **71** (2011) 1554, [Erratum: Eur. Phys. J. C 73 (2013) 2501],
arXiv: `1007.1727 [physics.data-an]`.

[140] A. L. Read, *Presentation of search results: the CL_s technique*, J. Phys. G **28** (2002) 2693.

[141] ATLAS Collaboration, *Constraints on new phenomena via Higgs boson couplings and invisible
decays with the ATLAS detector*, JHEP **11** (2015) 206, arXiv: `1509.00672 [hep-ex]`.

[142] Q.-H. Cao, Z. Li, J.-H. Yu and C.-P. Yuan,
Discovery and identification of W' and Z' in $SU(2)_1 \otimes SU(2)_2 \otimes U(1)_X$ models at the LHC,
Phys. Rev. D **86** (2012) 095010, arXiv: `1205.3769 [hep-ph]`.

[143] K. Y. Lee, *Lepton flavor violation in a nonuniversal gauge interaction model*,
Phys. Rev. D **82** (2010) 097701, arXiv: `1009.0104 [hep-ph]`.

[144] K. Y. Lee, *Unitarity violation of the CKM matrix in a nonuniversal gauge interaction model*,
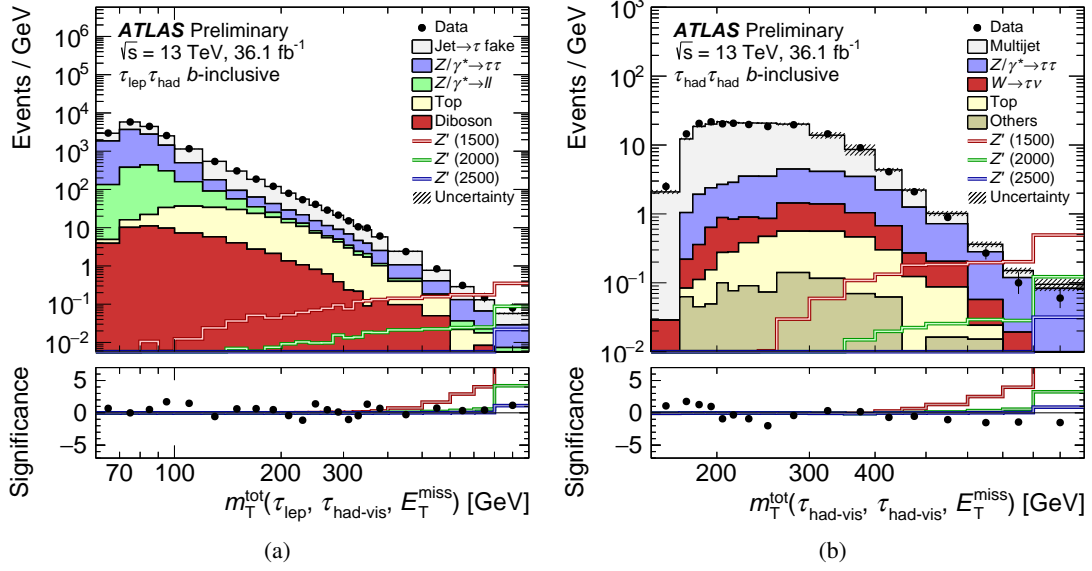Phys. Rev. D **71** (2005) 115008, arXiv: `hep-ph/0410381`.

Appendix

Figure 11: Post-fit $m_{\mathrm{T}}^{\mathrm{tot}}$ distributions for the b-inclusive selection in the (a) $\tau_{\mathrm{lep}}\tau_{\mathrm{had}}$ and (b) $\tau_{\mathrm{had}}\tau_{\mathrm{had}}$ channels. The expectation from Z'_{SSM} with masses of 1500, 2000, and 2 500 GeV are superimposed.

(a) $\phi \to \tau\tau$ (gluon fusion)

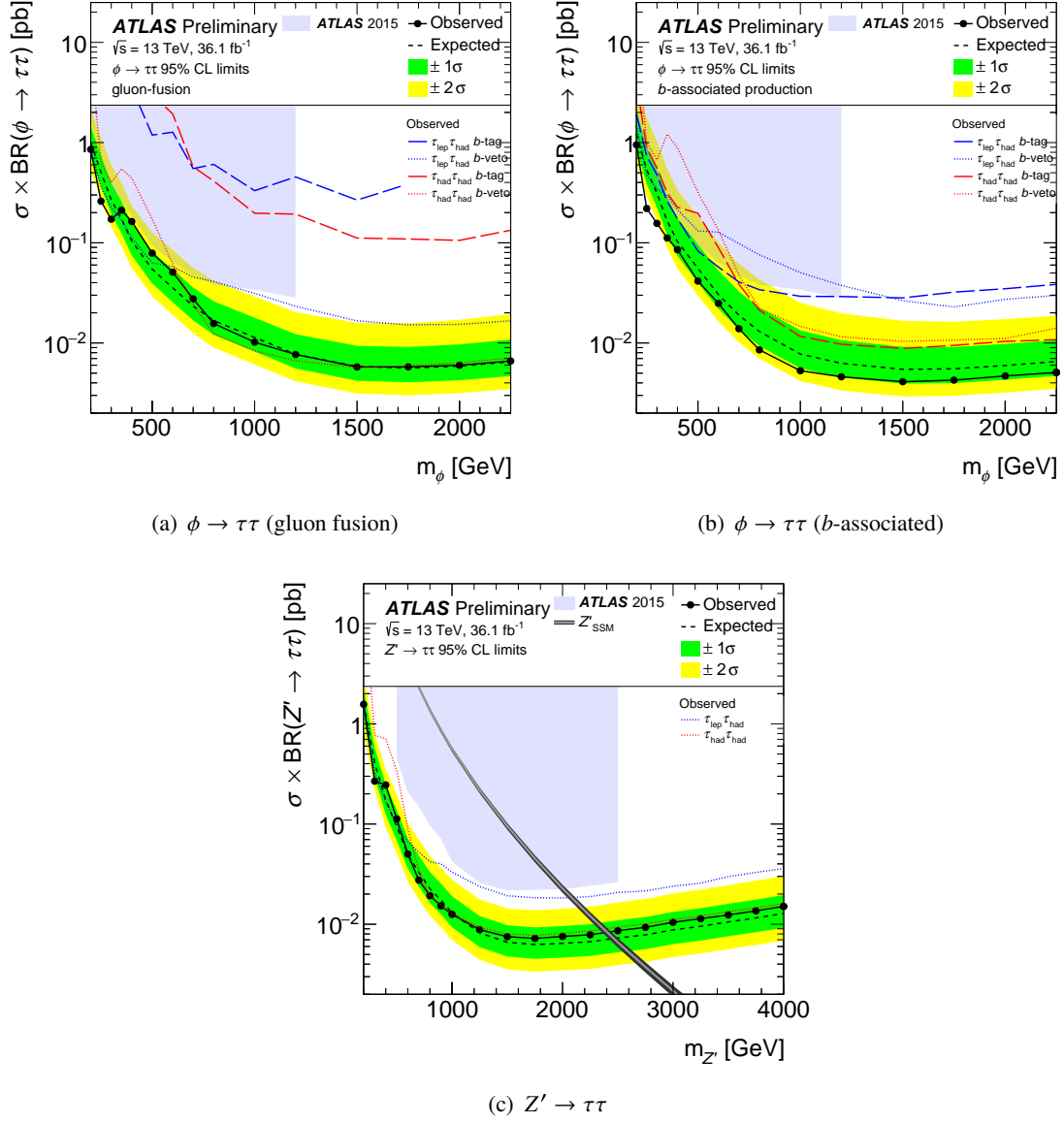(b) $\phi \to \tau\tau$ (b-associated)

(c) $Z' \to \tau\tau$

Figure 12: The observed and expected 95% CL upper limits on the production cross section times ditau branching fraction for a scalar boson produced via (a) gluon fusion and (b) b-associated production and for (c) gauge bosons. The limits are calculated from a statistical combination of the $\tau_{lep}\tau_{had}$ and $\tau_{had}\tau_{had}$ channels. The predicted cross section for a Z'_{SSM} boson is overlaid in (c). For comparison, the observed limits for the individual channels and categories and the observed limit from the ATLAS 2015 search [31] are overlaid.